REPORT DOCUMENTATION PAGE

Form Approved
OMB NO. 0704-0188

1. AGENCY USE ONLY (Leave blank)	2. REPORT DATE	3. REPORT TYPE AND DATES COVERED
	12/23/2003	Final Progress Rept. 01 Jun 98 - 30 Nov 03

4. TITLE AND SUBTITLE
Adaptive Optoelectronic Eye

5. FUNDING NUMBERS
DAAG55-98-1-0288

6. AUTHOR(S)
Pallab Bhattacharya

7. PERFORMING ORGANIZATION NAME(S) AND ADDRESS(ES)
Solid State Electronics Laboratory
Department of Electrical Engineering and Computer Science
University of Michigan
Ann Arbor, MI 48109-2122

9. SPONSORING / MONITORING AGENCY NAMES(S) AND ADDRESS(ES)
U.S. Army Research Office
ATTN: AMSRL-R0-S (IPR)
PO Box 12211
Research Triangle Park, NC 27709-2211

10. SPONSORING / MONITORING AGENCY REPORT NUMBER
38550-EL-MUR
.14

11. SUPPLEMENTARY NOTES
The views, opinions and/or findings contained in this report are those of the author(s) and should not be construed as an official Department of the Army position, policy or decision, unless so designated by other documentation.

12a. DISTRIBUTION / AVAILABILITY STATEMENT
Approved for public release; distribution unlimited.

12b. DISTRIBUTION CODE

13. ABSTRACT (Maximum 200 words)

The objective of this multidisciplinary research program was to develop a versatile image sensor technology where advances in optical devices and merging of optoelectronics, micro-optics and micromechanical components would allow the feasibility of tightly coupled adaptive focal plane arrays. We adopted a layered architecture in which the essential elements were: The front-end optics consisting of a variable focus Fresnel lens, a microlens array and a microprism array for color dispersion and adaptation: photoreception and transmission array consisting of low-power and high-power phototransceiver arrays; and information processing with vertical fan-out via multiple-stacked SiGe/Si photoreceivers. A dual focus Fresnel lens and micromachined platform for steering optical elements were demonstrated. A color adaptation model was tested with micromachined platforms. We designed, fabricated and demonstrated novel microcavity LEDs and VCSELs with quantum well and quantum dot active regions. These devices have been used to realize ultra-low power phototransceivers (10 nW input power, 110μW power dissipation) with 18 dB gain. This is the first demonstration of an ultra-low power phototransceiver which can be used in dense arrays for imaging applications. We have also demonstrated multi-channel SiGe/Si photoreceiver arrays with ≥ 1 GHz bandwidth for electronic processing of the optically imaged signals.

14. SUBJECT TERMS			15. NUMBER IF PAGES
			16. PRICE CODE
17. SECURITY CLASSIFICATION OR REPORT	18. SECURITY CLASSIFICATION OF THIS PAGE	19. SECURITY CLASSIFICATION OF ABSTRACT	20. LIMITATION OF ABSTRACT
UNCLASSIFIED	UNCLASSIFIED	UNCLASSIFIED	UL

Final Report

On

Adaptive Optoelectronic Eye
(Multidisciplinary University Research Initiative)

Grant: DAAG 55-98-1-0288

Period

06.01.1998 – 11.30.2003

Principal Investigator

Professor P. Bhattacharya

Department of Electrical Engineering and Computer Science

University of Michigan, Ann Arbor, MI 48109-2122

pkb@eecs.umich.edu

Co-Principal Investigators

Professor D. Deppe, University of Texas, Austin

Professor G. I. Haddad, University of Michigan

Professor S. W. Lee, University of Michigan

Professor C. T-C. Nguyen, University of Michigan

December 2003

FOREWORD

The final report of the ARO-MURI program on the Adaptive Optoelectronic Eye is enclosed. Researchers from the University of Michigan, Ann Arbor and the University of Texas at Austin were involved in this program of research. The overall project objective was to develop key components and technologies suitable for adaptive vision and similar sensing applications. To this end, we have developed novel devices and components, suitable for such applications. Technical oversight of the program was provided by an Executive Advisory Board and a Technical Advisory Board.

TABLE OF CONTENTS

1. STATEMENT OF THE PROBLEM STUDIED

There is a need to develop an agile sensor technology for surveillance, detection and image recognition. Such a technology should be able to detect, process and transmit near-perfect optical images and related information that would adapt automatically to changing scenarios and environments. The biological eye is the most perfect adaptive sensor that performs these functions. To realize functions of vision, it is necessary to process a large capacity of information at high speed. The eye and retinal functions, which would require extraordinary high signal bandwidth or massive parallel feed-forward or feedback channels with multiple fan-outs between the pixel elements of the focal plane, cannot be realized with present-day hard-wired microelectronics and VLSI technology. In order to realize and adaptive eye, it is imperative to take recourse to optical processing, benefiting from two well-known attributes of light waves: they can be transmitted in parallel without interference and they have much higher information carrying capacity. The ideal configuration of such an adaptive optical or optoelectronic eye is a coupled layered focal plane structure with local processing cells.

The objective of this program is to develop a versatile image sensor technology where advances in optical devices and merging of microelectronics, microoptics and micromechanical components would allow the feasibility of tightly coupled adaptive focal plane arrays.

The essential elements of the layered architecture are:

1. A front-end and large variable focus Fresnel lens that focuses the image on a microlens array. Each microlens focuses light on a single steerable microprism for color dispersion. These separate colors impinge on multiple detectors in each pixel of the low-power phototansceiver.
2. Photoreception and transmission in an array. The pixel size is limited to approximately 500μmx500μm and we have to think of an eventual technology involving 10x10 and 100x100 arrays, power requirements and heat dissipation for

4 phototransceivers in each pixel will be a problem. To alleviate this, we will have two separate phototransceiver chips: a low-power and a high-power. In the first, each pixel will have 4 phototransceivers consisting of a high-sensitivity phototransistor, which drives a microcavity LED or a low threshold VCSEL. The objective is to amplify and re-transmit (possibly at a wavelength different from the incoming wavelength) 4 colors from each pixel, with the input power being of the order of 1μW and the electrical power consumption not to exceed 300-400μW per color. Therefore the total power consumption per pixel is 1.2-1.6mW. There are no speed/bandwidth requirements of the low-power phototransceiver chip. In the following high-power phototransceiver chip, a TDM scheme is employed, where the photocurrent from several front-end photodiodes over several pixels is successively amplified by one transimpedance amplifier (consuming 10-30mW power) and the amplified photocurrent drives a high-speed VCSEL. It is envisaged that the input and output optical powers would be 50-100μW per detector and 0.5-1mW per VCSEL, respectively. We will not demonstrate the TDM switching scheme, but only the photodiode, amplifier and VCSEL integration.

3. Processing of information with Si-based CMOS and vertical/lateral fan-out. Hence, we will only demonstrate photoreception in multiple stacked chips with Si/SiGe photoreceivers.

In what follows, the significant accomplishments of the program, in the different areas, are highlighted.

2. Summary of Most Important Results

2.1. Dual-Focus Quantum-Well Fresnel Lens Modulator

Image sensor technologies being envisioned at the present time will utilize advances in optics, optoelectronics, and micromechanical components for application in adaptive focal plane arrays and even in the adaptive optoelectronic eye. An

optoelectronic version of a possible adaptive eye is shown in Fig. 1. The first optical element in such a scheme would be a variable focus, or dual focus, lens which is compact and steerable. It would be advantageous to realize the lens with semiconductor materials, so that processing electronic and optoelectronic components can be incorporated on the same chip, if necessary. Bragg-Fresnel lenses and Fresnel-zone plate type of lenses have been fabricated on GaAs substrates for focusing X-rays. By making such lenses with an electro-optic material, such as PLZT ceramic or liquid crystal, dual-focus lenses have been demonstrated. In this project, we have designed and demonstrated a dual focus Fresnel lens made with GaAs/AlGaAs multiple quantum wells, wherein the quantum-confined Stark effect (QCSE) is utilized to change the focus. To the best of our knowledge, this is the first demonstration of a quantum well based (semiconductor) Fresnel lens.

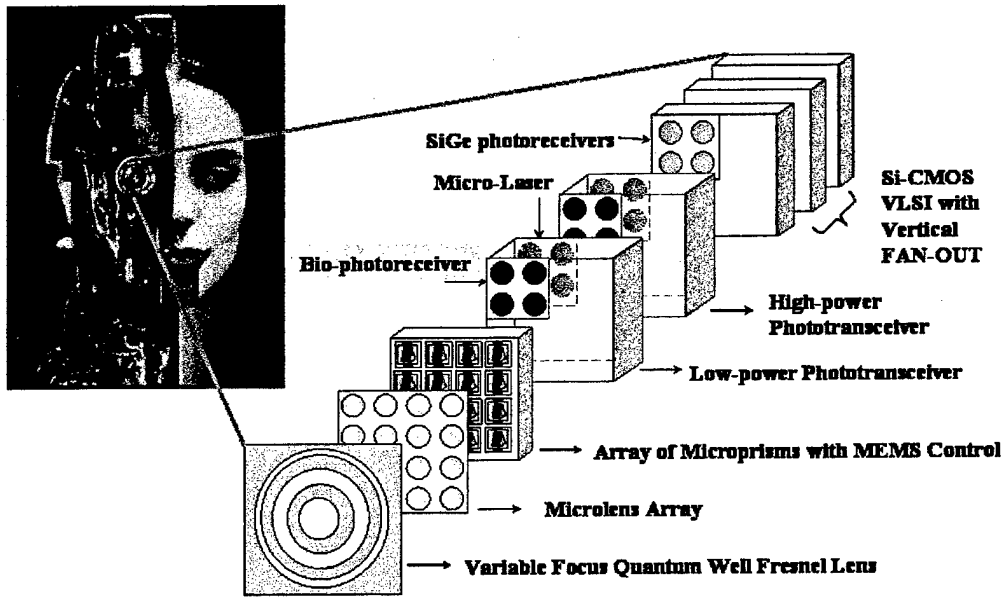

Fig. 1: Schematic of an artificial vision system incorporating a MQW Fresnel lens and a bio-photoreceiver array.

The Fresnel zone plate consists of a series of alternate transparent and opaque rings, or zones. The radii of the rings are so chosen that a parallel beam of light passing through these zones interferes constructively to produce a focus. The operation of the MQW Fresnel lens is based on the change in multiple-quantum-well absorption with a

reverse bias. The phase difference of the light path between two adjacent zones is arranged to be 2π and, by arranging the light wavelength to coincide with the zero-bias MQW absorption peak, a certain amount of unfocused light is transmitted with zero bias applied across alternate zones. With the application of a reverse bias across alternate zones, these zones are rendered more transparent due to the decrease of absorption by QCSE and a focus is obtained at a point $f = 2r_1^2 / \lambda$, where r_1 is the radius of the first zone. With the change in absorption coefficient, $\Delta\alpha(V)$, there is an accompanying change in phase, $\Delta\Phi = \Delta n_r(V) k_\circ d$ (where $k_\circ = 2\pi / \lambda$), due to the electro-optic effect in the MQW; but this effect will be small. Thus a dual focus lens-modulator is realized.

Fabrication of the Fresnel lens is initiated with the deposition of transparent indium tin oxide (ITO) on top of the p^+ GaAs layer, to serve as the p-type ohmic contact. It is then mounted face down onto a glass plate with epoxy and the GaAs substrate is selectively removed by wet chemical etching. n-type ITO ring contacts are formed by photolithography and lift-off and mesa etching is done down to the superlattice region, so that deep grooves are formed between the rings (Fig. 2). The depth of the grooves is adjusted to provide a phase shift of 2π between the optical paths of the neighboring zones. The radius of the first Fresnel zone was chosen to be 147 nm so that the focal length would be 2.5 cm at λ = 860 nm. The results reported here are from lenses of dimension 1.01mm × 1.01mm having 25 rings.

For measurement of transmitted intensity, light from a diode laser (λ = 859 nm) was collimated by a beam expander and was impinged normally upon the Fresnel lens. The transmitted beam in the z direction was measured by a Micronviewer CCD camera (Model 7290A) from Electrophysics Inc. The spot size of the beam impinging on the lens was around 0.5cm × 0.5cm. The measured transmission of light, as a function of bias, is shown in Fig. 3.The small amount of light seen in the center in Fig. 3(b) is believed to be due to an imperfect phase condition caused by the ITO deposition on alternative rings. Our result clearly demonstrates the expected dual-focus behavior of the Fresnel lens-modulator. The insertion loss of the lens was measured to be 5dB.

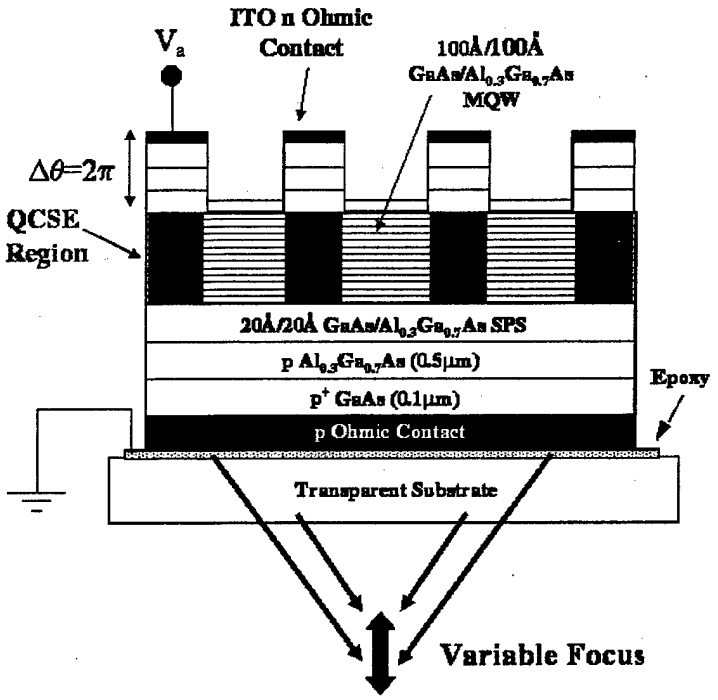

(a)

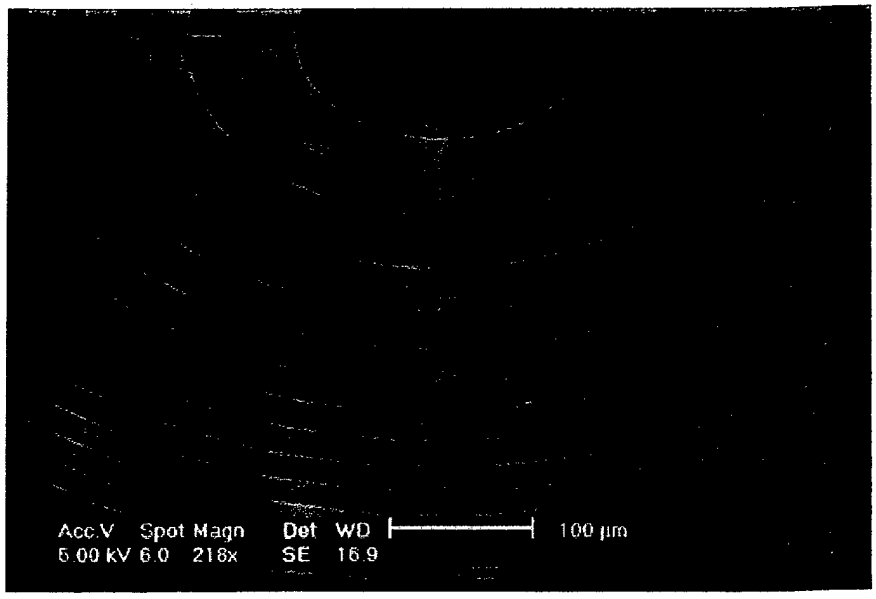

(b)

Fig. 2: (a) Schematic and (b) photomicrograph of the fabricated MQW Fresnel lens device structure.

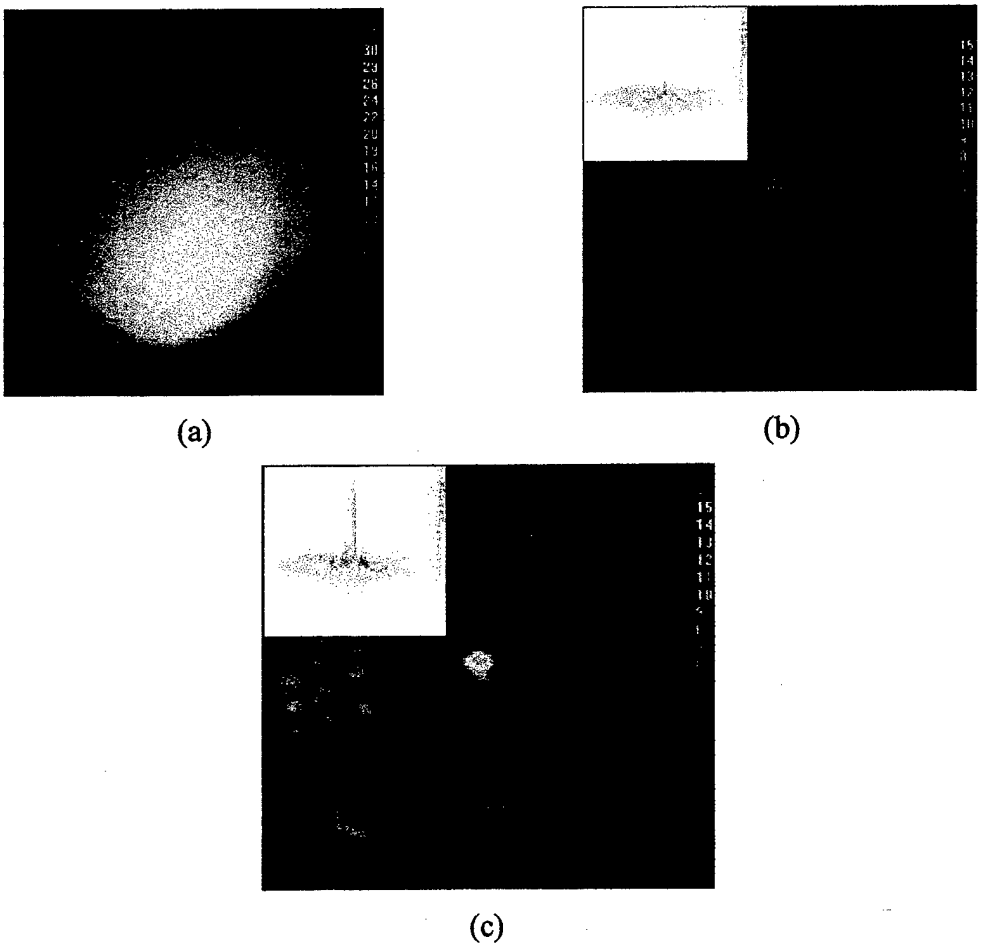

(a) (b)

(c)

Fig. 3: CCD image of the collimated 859nm light at focal plane (a) without the insertion of lens (b) with zero bias applied to lens (c) with –12 V applied to lens.

To explore the potential of variable focus with this type of electro-optic MQW Fresnel lens, we fabricated two lenses with focal lengths of 2 cm and 5 cm, respectively, and stacked them together. With the experimental set-up presented in Fig. 4, preliminary experiments were conducted to test the combined focusing effect. The two MQW Fresnel zone plates were aligned in parallel along the same normal axis. A distance of 1cm was left in between for probe contacting. When bias voltages were applied onto each lens separately, two main focal planes were observed behind the second lens in the direction of the transmitted light. The first plane is 2 cm away from the second lens surface, while the other is 4 cm away (Fig. 4). Our observation indicates that each lens of the stack generates its own focal plane in the space, with little influence from the other. This

conclusion is reinforced by the fact that the focusing strength in each plane only strongly varied with the applied voltage on its corresponding Fresnel lens. Our experiment thus demonstrates a switching of the focal length at 2cm, 4cm and ∞by biasing the Fresnel lens devices alternatively.

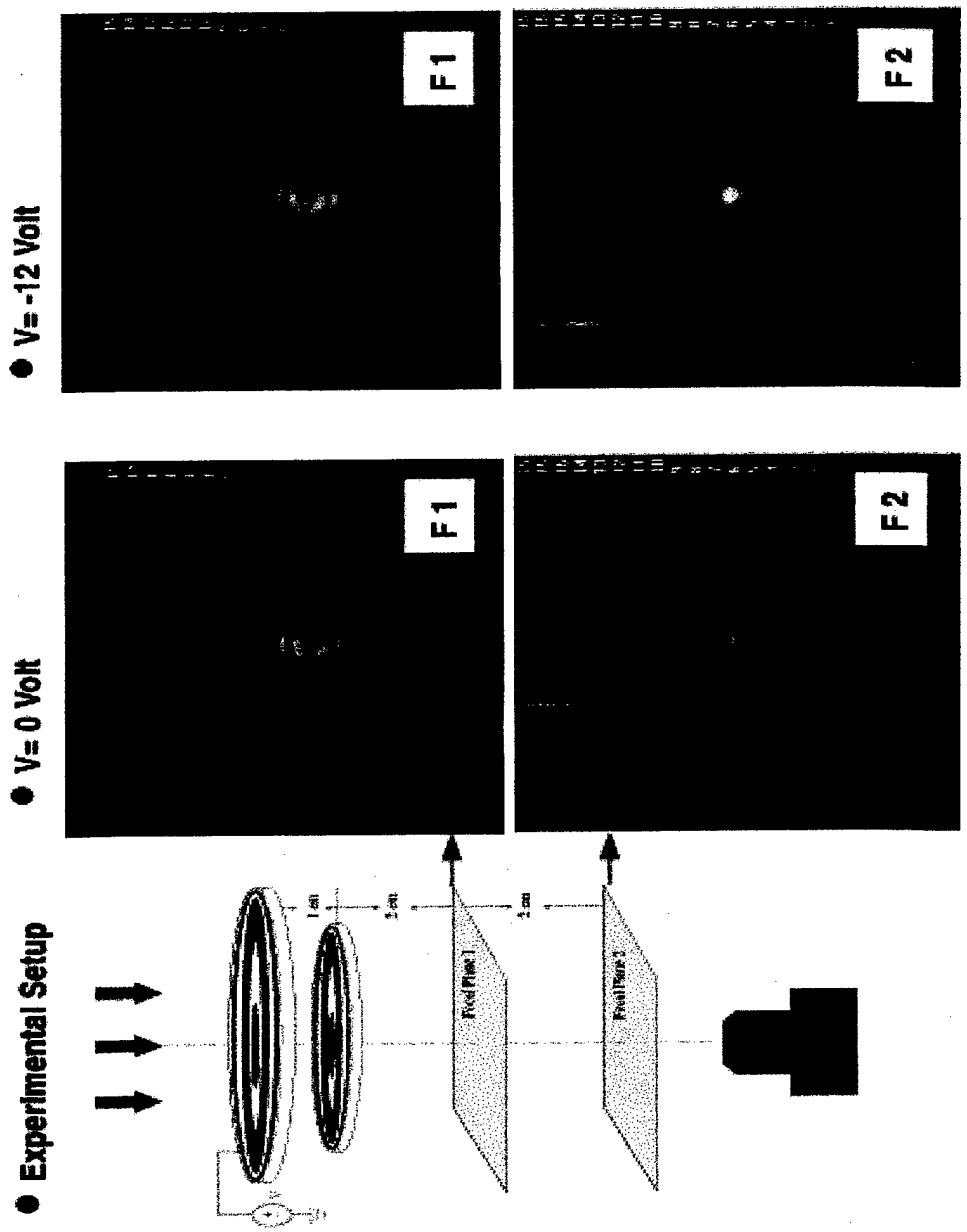

Fig. 4: Schematic of the experimental setup; and the CCD images of the variable focusing effect of the stacking MQW Fresnel lenses. Reverse bias was applied on the top lens with 5cm-focal length.

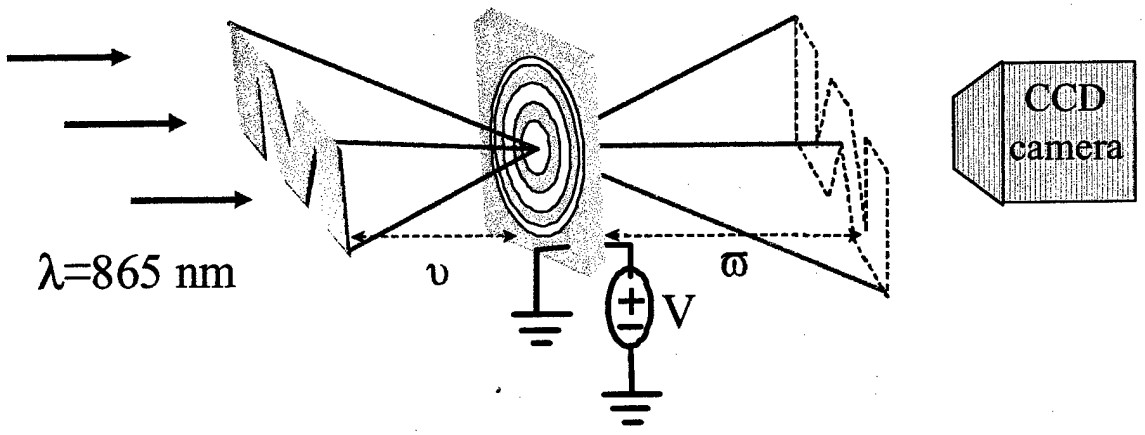

(a)

(b)

Fig. 5: (a) Experimental set-up (b) CCD pictures of the Fresnel Lens imaging effect under a reverse bias of 10 volts.

The imaging effect of the Fresnel lens with near-infrared light (λ = 860 nm) was also investigated. The results reported here are from lenses of dimension 1.01mm × 1.01mm having 25 rings, and a focal length of 2.5 cm. For the measurement, letters "U" and "M" were inversely printed on a transparency, which was then inserted into the path of a laser beam, about 4.5mm in front of the lens. With a CCD camera, we observed the inverted images of those letters forming at a plane about 3.5 mm behind the lens surface. Fig. 5 shows such images when the lens is biased at -10 volts. It was also found that the

relationship between the object distance (u), the focal length (f), and the image distance (v) followed the Gaussian form of the thin lens equation:

$$\frac{1}{u}+\frac{1}{v}=\frac{1}{f}. \tag{7.5}$$

With improved fabrication techniques, it is possible to remove the residual focusing effect, and eventually realize the switch between a Fresnel lens and a semi-transparent glass plate on our device.

In summary, a Fresnel lens-modulator made with MQW materials is presented. The lens demonstrates bias-dependent dual-focus behavior and a 7:1 ratio in focused intensity modulation. Further analysis indicates that this focusing effect is mainly due to the QCSE induced absorption change rather than the modification of refractive index. Variable focus was tested by stacking two MQW Fresnel lenses together. The switching of focal length between 2cm, 4cm, and infinity was observed in the preliminary experiment. The imaging effect of the MQW Fresnel lens was also tested. The relationship between the object distance, the focal length, and the image distance was found to follow the Gaussian form of the thin lens equation. Although the demonstration reported here is with near-IR excitation, the lens can, in principle, be designed for visible illumination, using wide-bandgap heterostructures.

2.2. High Efficiency Color Discrimination and Adaptation using Steerable Microprism Array

For visual object detection and recognition in surveillance, reconnaissance, and target detection, stable and reliable photometric features should be extracted from images and the features should represent the object properties without any influence from illumination colors and directions. Photometric descriptors invariant to lighting conditions in an adaptive manner can provide reliable features for geometric and photometric identification of objects.

Although color can carry powerful photometric signatures when objects or object features are distinguishable by their distribution of color reflectances, color information is highly susceptible to illumination conditions. To effectively employ color information as a reliable descriptor of an object, color reflectance intrinsic only to the object surface must be extracted. Variation of color appearance due to object shape, viewing, illumination pose and illumination color needs to be discounted.

2.2.1. Design of color discrimination schemes and optics/MEMS subsystem

In this project, we developed a comprehensive framework of interpreting and discounting image changes due to gloabal and local illumination color and direction, and designed a high-efficiency adaptive optoelectronic vision system based on the steerable MEMS microprism array. The development of adaptive vision models in conjunction with the state-of-the-art optoelectronic and MEMS technology has been unprecedented.

2.2.2. Development of color adaptation models/algorithms

(a) Spectral Gradient (SG):

When spatially uniform illumination color varies in time, an object's color signatures based on usual red, green and blue channel values are deformed and object recognition becomes difficult. Our approach forms a global illumination-invariant representation by taking spectral derivatives of logarithmic colors. The color descriptors in the resulting log-chromaticity space facilitates the analysis and interpretation of image color change due to illumination and reflectance. The spectral gradients of an object are not deformed due to the illumination color, but shifted uniformly in the log-chromaticity space. This allows stable color recognition and estimation of illumination color change. The spectral gradients are not invariant to spatial variation of illumination.

(b) Spectro-Spatial Gradient (SSG):

We further investigate spatial derivatives of the spectral gradients to achieve a degree of invariance to local spatial variation of illumination color. Most of the existing illumination-color/pose invariants have not been specifically developed to be invariant to the degradation of color matching due to locally varying illumination color. The spectro-spatial gradients can be used in an additional stage of color matching for detecting potentially good matches that cannot be caught by spectral gradients alone due to local irregularities in illumination color.

(c) Adapted Spectral Gradients (ASG):

Due to its invariance to spatial and temporal variation of illumination color, the discriminating power of SSG is somewhat decreased compared to SG. Our approach to this problem is to estimate the illumination variation across the scene in an image and flatten the illumination color. This adapted spectral gradient from the illumination-flattened image can be regarded as spectral gradient under uniform illumination color. The ASG is invariant to spatial and temporal variation of illumination color, and its descriptive power is as high as SG.

2.2.3. Feasibility study: extension of spectral gradients to Long-Wave Infrared

The visual features in the long-wave infrared (LWIR) range not only depend on emissivity intrinsic to an object but on the object's temperature. We investigated the extension of spectral gradients to LWIR for an object's invariant descriptor to temperature, and from this feasibility study, we developed spectral gradients in the form of logarithmic irradiance ratio in LWIR. Since there are many complex scattering and reflection terms in short-wave and mid-wave IR, the feasibility study is limited to the long-wave IR where only thermal radiation matters without complex scattering and reflections.

2.3. STEERABLE MICROPRISM ARRAYS

In this part of the project, we designed, fabricated and tested an MEOMS (micro-electro-optical-mechanical system) device. The target of the system is to disperse the color content of the incoming light and modulate the colors from pixel to pixel on the detection plane—an operation often required by algorithms for color adaptation in vision systems. A microprism and an electrostatic tiltable microplatform are chosen as the dispersive device and as the actuator, respectively. In addition to those two components, a group of microlenses is used to receive the light at the front-end of the system. The system is compact and three-dimensional.

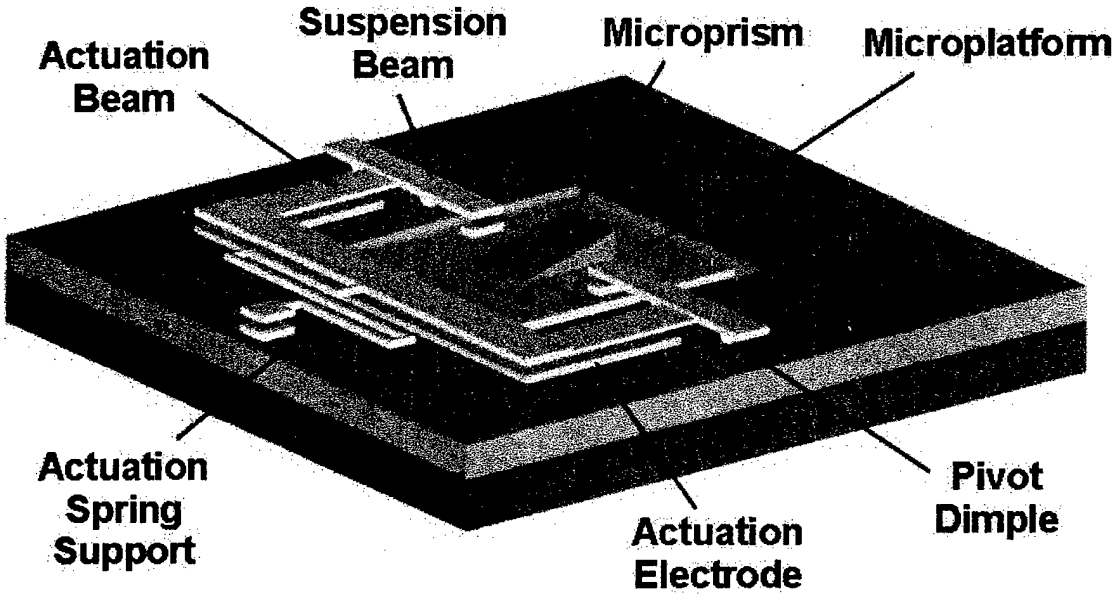

Fig. 6: 3-D view of steerable microprism.

In the first generation of the design, large diffraction of the light exists in the system, which in the end will result in the overlapping of the dispersed colors. The metal-based fabrication process is relatively simple but unstable, causing very low yield of the devices. In the second generation of the design, the diffraction is greatly minimized by placing the photo detector closer to the microprism than before. A material with very high refractive indices is used for the prism to ensure more widely dispersed color within a shorter distance. On the other hand, because the change in the angle of light passing through a prism is only a weak function of the prism tilt, tilt angles of 10° or greater are

needed for adequate traversal of colors over adjacent pixels, and such tilts must be accomplished via low voltages and with low power consumption. A tiltable microplatform with a novel bent-beam actuation method is designed to satisfy the requirement. Fabrication process is changed to polysilicon-based LPCVD process which is much more robust than the previous one, so high yield of the devices is achieved.

The details on the operation, design, fabrication and test of the microplatform are described as follow.

1. The low-stress nitride microplatform itself is suspended via rigid polysilicon suspension beams above a hole in the silicon substrate that (1) allows light to pass through; and (2) allows unimpeded tilting of the microplatform over very large angles. The suspension beams are actually not anchored to the substrate directly, but rather rest upon the substrate via strategically-placed dimples, around which the suspensions can pivot to affect tilting of the platform. These pivoting suspension beams together with the network of beams attached to them then realize the bent-beam actuation mechanism that makes possible tilting of the platform at such low voltages. Bent-beam actuation is achieved by pulling down a thin doped-polysilicon beam perpendicularly attached to the suspension beam, and bending this thin beam close to the suspension dimple so as to pivot the suspension around an angle defined by the degree of bending in the thin beam. In this work, the thin beam is pulled down electrostatically by applying a suitable voltage to an underlying, nitride-covered (to prevent shorting), doped-polysilicon electrode. The voltage required to achieve a given angle is greatly reduced in this system, because: (1) the pivoting dimple eliminates the need to overcome a torsional stiffness; and (2) once pulled down, portions of the beam near the bend are very close to the underlying electrode, so the electrostatic beam-bending force is larger for a given voltage. To obtain an expression for tilt angle as a function of applied actuation voltage for a bent-beam actuator, an energy method in mechanics is used.

2. The microplatform is first fabricated on a silicon wafer by the surface micromachining technology. The microprism is then delineated by exposing the photo resist through a gray-scale mask that affects a linear variation in exposure intensity over the prism area, effectively exposing a triangular shaped cut into the photo resist thickness. A subsequent development step then removes all exposed photoresist, leaving behind a photoresist microprism. A dry etching step is then used to transfer the photoresist microprism mold to the material having the high refractive indices. To allow the passage of light through the microprism, a through-wafer hole is etched from the back side of the wafer using the Bosch process before release. The release etch is finally done using concentrated HF, followed by a supercritical CO_2 drying step to minimize sticking.

3. Completed microplatforms were tested using three different methods: (1) direct visual observation in air under an optical microscope; (2) observation under an SEM equipped with electrical feedthroughs; and for the best accuracy, (3) the optical measurement setup depicted in Fig. 6. In the last of these, the sample under test is mounted on an xyz-stage and a He-Ne (532nm) laser beam is focused on the microplatform using an objective lens with a focal length of 50mm. The reflection of the laser beam from the platform is projected onto a white screen with a measurement scale, from which the tilt angle of the microplatform can be extracted using trigonometric identities together with the law of reflection. Measurement results show that microplatforms are able to achieve DC tilt angles larger than 10° with actuation voltages less than 20V, and a resonance tilt angle of 19° when driven to resonance at 33 kHz via a combination of 14V DC, plus 5V AC.

An electrostatic bent-beam actuated tiltable microplatform housing a microprism, fabricated using a combined surface micromachining with deep RIE technology and phase lithography has been demonstrated and the static and dynamic characteristics have been measured. Given that the described bent-beam actuation technique is largely electrostatic in nature, the tilt angle-to-voltage/power ratio achieved by the above values represents one of the largest available using MEMS technology. This, combined with an

implementation structure conducive to transmission-based optical signal processing, makes the device a good candidate for 3D arrayed adaptive vision applications. In this regard, the tiltable dispersive microprism function of this device is presently under evaluation.

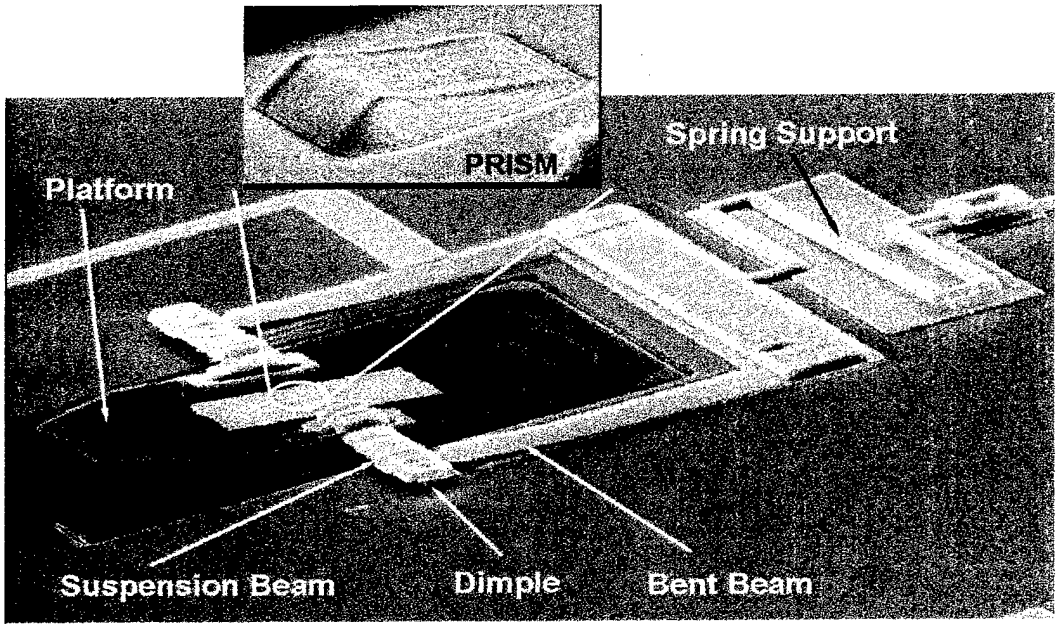

Fig. 7: 100x90μm^2 microplatform housing a photoresist microprism.

2.4. COLOR SEPARATION USING FREQUENCY SELECTIVE SURFACES

The goal of this portion of the project was to implement frequency selective surfaces for color separation in electro optical eye applications. Frequency selective surfaces are planar structures with a regular array of opening that can be designed to produce a frequency response at millimeter wave or optical frequencies. The advantage of these structures is that the frequency response depends on the dimensions and spacing of the openings in the array and not on a layer thickness as in other optical filters. A range of filter characteristics can be realized in a single surface by varying the pattern. This simple fabrication greatly reduces the complexity of integration into an optical system. This project investigated the design, fabrication an experimental characterization of these FSS structures.

The first step in the project was to gain information on FSS structure design. Although a variety of simple analytic expressions are available, computer simulations are needed in obtain accurate information. Simple planar structures can be analyzed using method-of-moments simulations. This approach was used early in the project. However this approach doesn't allow finite thickness layers. This causes 2 problems. First the MOM code has problems with the analysis of AR coatings with a thickness approaching a wavelength. Second the MOM approach doesn't handle finite conductivity materials. These problems can be solved by using a boundary element FEM code combined with a MOM. This technique was used to accurately predict structure response. An example simulation is shown in Fig. 8. This figure shows the wavelength response of FSS. The black line shows the response predicted by the MOM code. This assumes zero metal thickness and infinite conductivity. However thin gold layers are semi transparent at optical frequencies. This must be accounted for in the simulation. The 10 nm layer curve shows almost no wavelength response. The 30 nm layer has a reasonable wavelength response although it is shifter to longer wavelengths. This figure also shows the effect of finite layer thickness. The holes in the metal pattern are less than ½ in diameter, forming small waveguide below cutoff cylinders. Increasing the layer thickness increases the attenuation and reduces the transmission. The 100nm structure transmission has been reduced to 20%. These effects need to be included in the FSS modeling in order to accurately predict performance.

The next step is to fabricate the structures. The small structures require electron beam lithography and a two level liftoff. Several earlier process sequences produced poor results. The main problem was poor liftoff with a lot of metal remaining on the surface. We recently started using a new electron beam lithography tool newly available in The Solid State Electronics Laboratory. This tool, combined with improved process characterization is now producing excellent FSS patterns. The new patterns are also nearly twice the size of the earlier structure. The larger structures are much easier to align in the measurement system. A small portion of a new pattern is shown in Fig. 9.

The final step is measurement and characterization. The FSS structures are characterized using a SOPRA GESP-5 Spectroscopic Ellispometry System. We are obtaining much better measurements due to the ease of alignment of the larger samples. A sample measurement is shown in Fig. 10. There is a good match between the measurements and the simulations.

Although we are now able to design, fabricate and characterize the FSS filters there are still several problems to overcome. We need to improve the band center transmission. This should be helped with an AR coating. The new software is being used to investigate this design. The filters have a reasonable long wavelength response, but the response is poor at shorter wavelengths. We are investigating several approaches to solve this problem including modified AR coating and multi layer stacks with dielectric spacers. The final task will be to combine these filters with detectors developed elsewhere in the program and to show color separation.

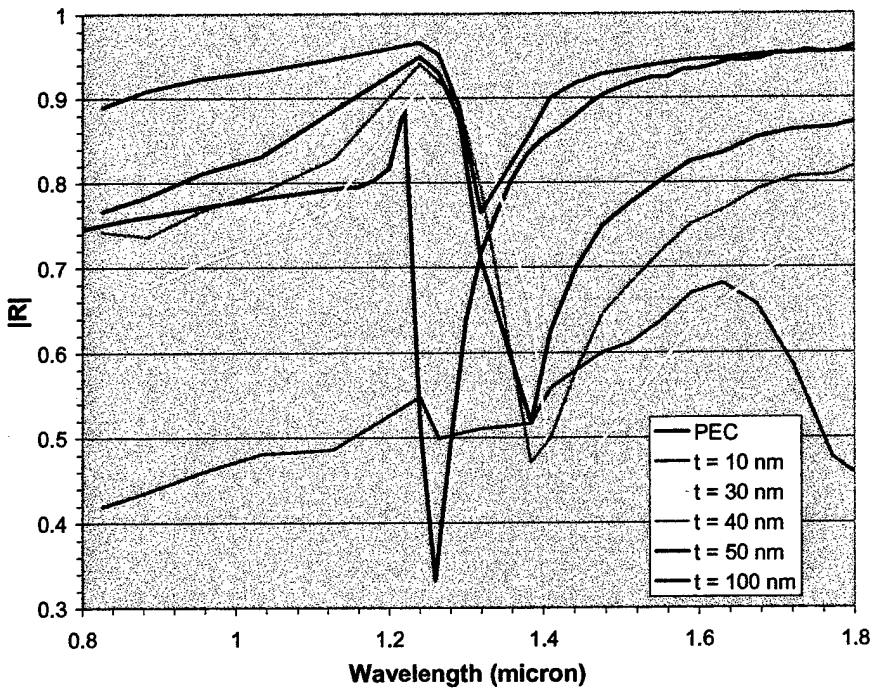

Fig. 8: Modeled metal thickness dependent performance.

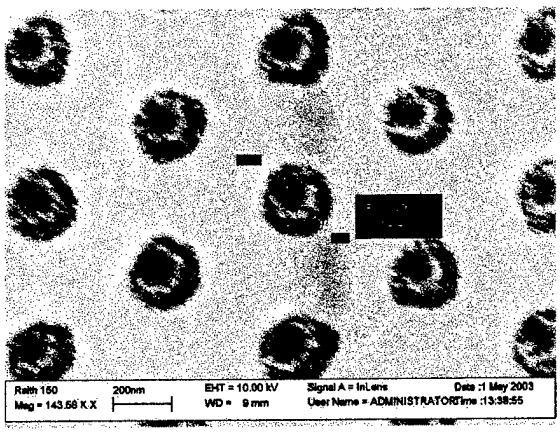

Fig. 9: Experimental Frequency Selective Surface structure with hole diameters approximately 100nm.

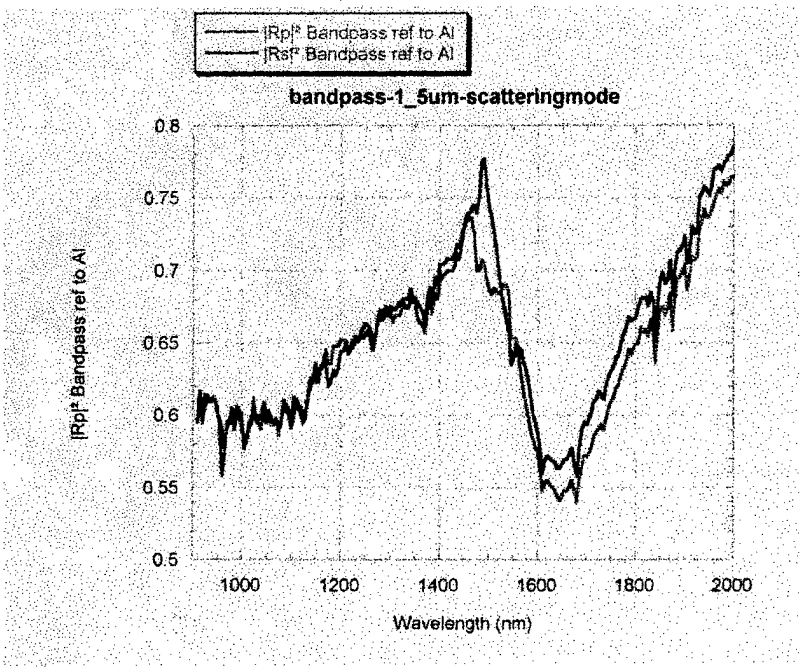

Fig. 10: Frequency Selective Surface Spectroscopic Ellipsometry characterization.

2.5. MICROCAVITY LIGHT SOURCES FOR LOW-POWER PHOTOTRANSCEIVERS

Densely-packed pixel transceivers are key elements for detecting, transmitting, and processing data for an adaptive optoelectronic eye. Because slower pixel speeds can be used for the highly parallel data processing based on dense optical interconnects, the

key requirements of such pixels are high efficiency and low power. Power consumption per transceiver pixel of less than ~100μW is useful to obtain the high packing density. To obtain the high efficiency requires ultralow threshold VCSELs or high efficiency microcavity light emitting diodes (MCLEDs). In the course of this program we showed theoretically that quantum dot (QD) MCLEDs can in principle provide the necessary speed and efficiency at the power levels needed for the low power transceiver chips. The QD MCLED is based on the Purcell effect that both shortens the radiative lifetime and improves efficiency in a single mode LED. This Purcell effect has been demonstrated in an apertured QD MCLED very similar to a VCSEL. This type of microcavity can obtain high efficiency in the output coupling from a single cavity mode, and our most recent experiments have focused on demonstrating a similar current injection device.

The Purcell effect was demonstrated in current injection QD MCLEDs in this MURI project (Zou et al., 2001 in list above). Although the overall efficiency was only ~1%, this was limited by nonradiative recombination. However, the efficiency dependence on aperture size shows that these types of LEDs can obtain efficiencies exceeding 20% or more when optimized, and at very low power levels and therefore have unique microcavity physics ideally suited to dense integration. The experimental results show that as the size of the aperture of the QD MCLED is reduced from 4μm to 3μm to 2μm to 1μm the efficiency consistently improves. From the 4μm aperture diameter to the smallest ~1 μm the efficiency improves by more than a factor of two. However, nonradiative recombination limits the maximum efficiency ~1.6%. Further improvements in QD material and cavity design should lead to the high efficiency at microwatt power levels. The improvement in efficiency was demonstrated for lower temperatures, with a maximum value of 16% achieved for relatively large apertures (Chen et al, 2001)

The microcavities described above are based on selective oxidation of AlGaAs. Although the oxidation results in high index contrast structures, the strain due to the oxide is a problem for reliability and yield. In our recent work on this program we have developed a novel cavity approach to realize similar microcavities based on air-gaps. The air-gaps provide even higher index ratios without strain. The cavity is based on air

gap/semiconductor Bragg reflectors that have the potential to ultimately increase the mirror reflectivity in a VCSEL, and decrease the total epitaxial layer thickness as well. Our first structures have used InGaAs planar quantum wells to test this cavity concept. An optical photograph of the device is shown in Fig. 13. The devices are grown using molecular beam epitaxy on a GaAs substrate. The active region, which contains three InGaAs quantum wells, is centered in a full-wave spacer. The bottom distributed Bragg reflector (DBR) consists of 31 n-doped GaAs/AlAs pairs. Two or three pairs of GaAs/air-gap DBR are used for top mirrors. Fig. 13 shows the top view of a device. Two rectangular windows are etched and the AlGaAs sacrificial layers are under etched after that. The shadow region in the picture shows the etched area in the AlGaAs sacrificial layers. High uniformity and yield are obtained with this two-step etch processing.

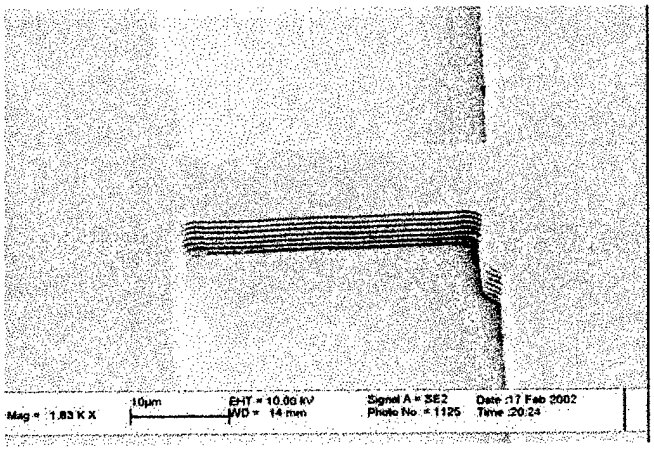

Fig. 11: Top view of air-bridge used to fabricate high contrast Bragg reflector containing quantum dot active region.

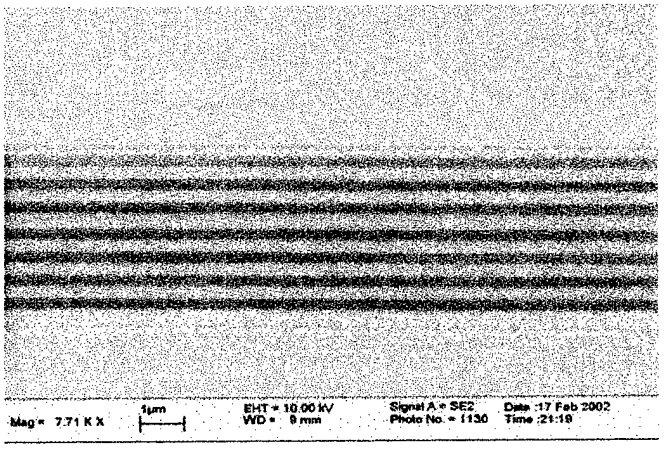

Fig. 12: Side view of vertical cavity using air-gap Bragg reflectors.

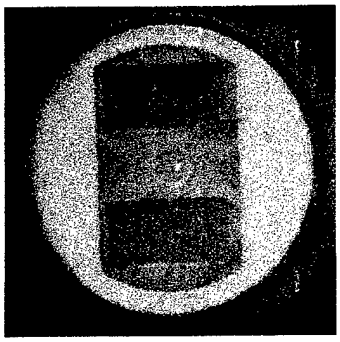

Fig. 13: Top-view of a VCSEL with GaAs/air-gap.

Continuous-wave room temperature lasing has been obtained using both 2 pairs and 3 pairs air-gap devices. The devices with 3 air-gap DBRs exhibit threshold current as low as 620μA. The corresponding threshold current density is 620A/cm^2. Differential quantum efficiency as high as 21% is achieved in our devices. We are presently working to develop this device concept for application to quantum dot active regions, including 1.3 μm sources. We believe this type of VCSEL provides an important platform for new device technology that will utilize the very low power potential of quantum dot active material. It also provides a microcavity approach that in principle provides the highest contrast possible in III-V structures, without strain effects. The photograph of Fig. 13 shows that, despite the air-gap mirrors, these types of devices can be scaled as well for dense photonic integration for use in optical chips such as needed for the optoelectronic eye.

2.6. Design and Development of Low-Power Phototransceivers

Dense arrays of low-power phototransceivers are required for imaging applications. In the adaptive optoelectronic eye, such an array will play a central role, in that it forms the first stage of the optoelectronic conversion with massive parallelism. Therefore, the low-power phototransceiver has some unique design criteria: small size, low power handling capability and low power dissipation. At the same time, speed of response and bandwidth are not important requirements. The challenge, therefore, was to integrate suitable combinations of photodetectors and amplifiers such that al, or most, of

these requirements are met. In the following, we describe the various OEICs that were developed in this program and imaging arrays of the phototransceivers.

2.6.1. Phototransceivers with Resonant Cavity Phototransistors and Microcavity LED or VCSEL:

A low-power phototransceiver can be realized by monolithically integrating a front-end phototransistor with a MCLED or VCSEL. The input signal is to be detected by a phototransistor in which the absorbing region is placed in a resonant cavity to improve the responsivity of light detection. The photogenerated current is then amplified by of β the HPT and then re-transmitted at a different wavelength by the microcavity LED. The parameters of both the resonant cavity phototransistor (RCHPT) and the LED should be optimized such that the chip is characterized by high optical gain, small chip size and low power dissipation. The active region of the RCLED consists of 3 $In_{0.18}Ga_{0.82}As$-GaAs quantum wells that form a λ-cavity and emit light at 0.94μm. The heterostructure and the confinement layer are designed to achieve high slope efficiency and low operating current. The top mirror of the microcavity LED is made with a MgF_2/ZnSe distributed Bragg reflector (DBR). In this integrated circuit both the MCLED and RCHPT share the bottom AlGaAs/GaAs DBR. The collector/absorber of the RCHPT is made of 9 $In_{0.12}Ga_{0.88}As$/GaAs quantum wells that detect 0.92μm input light. By using a resonant cavity HPT the effective absorption of the circuit can be increased and the photocurrent is internally amplified yielding high overall optical gain.

The HPT and MCLED/VCSEL are grown by molecular beam epitaxy in a single step. The phototransistor exhibits a responsivity of 60A/W at an input power of 1μW. The input and output wavelengths are 850 and 980nm, respectively. The MCLED-based phototransceiver exhibits an optical gain of 7dB and power dissipation of 400μW for an input optical power of 1.5μW. The small signal modulation bandwidth is 80MHz. On the other hand, the VCSEL-based phototransceiver exhibits an optical power of 10dB and power dissipation of 760μW for an input power of 2.5μW.

2.6.2. An Ultra-Low Power Phototransceiver

A low-power monolithically integrated phototransceiver consisting of a high-sensitivity modulated barrier photodiode (MBPD) and an $In_{0.4}Ga_{0.6}As/GaAs$ self-organized quantum-dot microcavity light-emitting diode, is demonstrated. The MBPD exhibits a responsivity of $1.8x10^3$A/W, for 630nm excitation, at an input power of 18dB and power dissipation of 110μW for an input power of 10nW. This is the first demonstration of an ultra-low power phototransceiver which can be used in dense arrays for imaging applications, meeting the requirements for power dissipation.

2.6.3. Vertically Integrated Phototransceivers

In order to reduce the size of the phototransceiver further, we have demonstrated a novel vertically integrated OEIC in which the two devices are integrated by a tunnel junction. This integration scheme simplifies processing and makes the area of the phototransceiver very small ($0.002mm^2$). We have successfully implemented phototransceiver arrays with these vertically integrated phototransceivers.

The equivalent circuit of the phototransceiver is shown in Fig. 14. The input optical signal is detected by the phototransistor in which the absorbing region is placed in a resonant cavity to improve the responsivity. The amplified photocurrent of the HPT drives the RCLED, which emits at a different wavelength. The optical gain of the phototransceiver is determined by the product of the phototransistor responsivity and current gain and the differential quantum efficiency of RCLED. As shown in Fig. 14, the tunnel junction provides a low resistance contact between n-doped emitter layer of the HPT and p-doped layer of the RCLED, through the distributed Bragg reflector (DBR) layers, which provide an optical isolation interface between the input and the output lights.

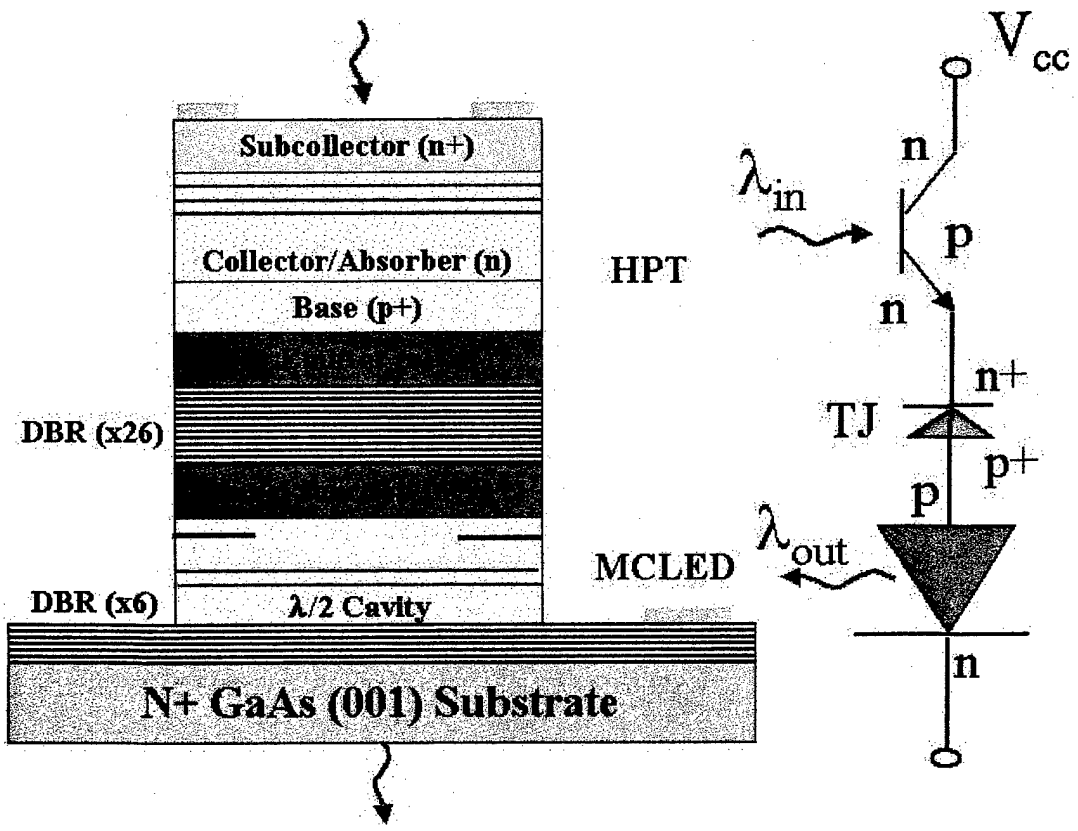

Fig. 14: Equivalent circuit and integration scheme.

The heterostructure was grown, in a single step, by molecular beam epitaxy (MBE). The layers are designed such that the light-absorbing MQWs in the HPT and emitting QW in the RCLED are placed at the antinodes of the optical field of the incident light and emitting light, respectively. The quantum well absorption peak occurs at 980nm, which coincides with the resonant frequency of the bottom DBR mirror. The base region is chosen to have a thickness of 100nm and a p-doping (with Be) of $10^{18}cm^{-3}$. The TJ was realized by degenerate C (p^{++}) and Si (n^{++}) doping. A ring contact is formed on the surface of the phototransistor (collector up) to enable photoexcitation. Mesa sizes of individual devices vary from 50-100μm in diameter. The aperture size (window opening) is defined by the area within the top ring contact; this varies in the range of 40-90μm.

The optical input-output characteristics of the phototransceivers were measured using a GaAs laser (λ=850nm), a tapered optical probe and a Ge detector. The optical gain of

the OEIC is a function of input power (i.e., photocurrent), which originates from the dependence of the current gain (β) of the HPT on the collector current. The measured optical transfer characteristics of a phototransceiver with a 90μm aperture size are shown in Fig. 15. As can be seen in the figure, the circuit exhibits an optical gain of 13dB at an input power of 5μW. The corresponding power dissipation of the circuit is 400μW.

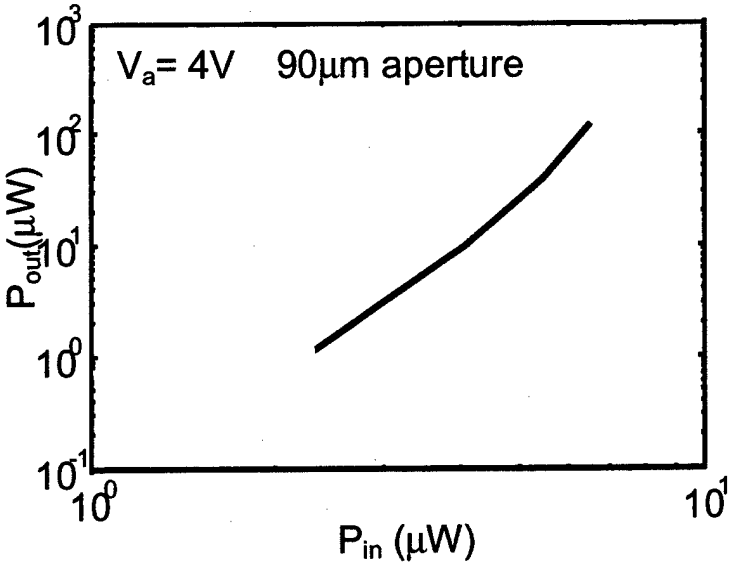

Fig. 15: Optical transfer characteristics.

The phototransceiver arrays demonstrate good uniformity, low optical crosstalk and imaging capabilities.

2.6.4. Imaging with Vertically Integrated Phototransceiver Arrays

As shown in Fig. 16, the vertically integrated phototransceivers demonstrate good spatial uniformity and are therefore suitable for the realization of dense imaging arrays. The adjacent channel crosstalk is also very small.

Phototransceiver arrays, ranging from 16x16 to 26x26 elements, were fabricated in order to demonstrate imaging capability of the vertical-integration scheme. A ring contact with annular radius of 2.5μm is formed on the surface of the phototransistor

(collector up) to enable photoexcitation. Individual mesas within the arrays with diameter 20μm to 40μm and spacing 40μm to 60μm were formed. The aperture size (window opening) is defined by the area within the top ring contact.

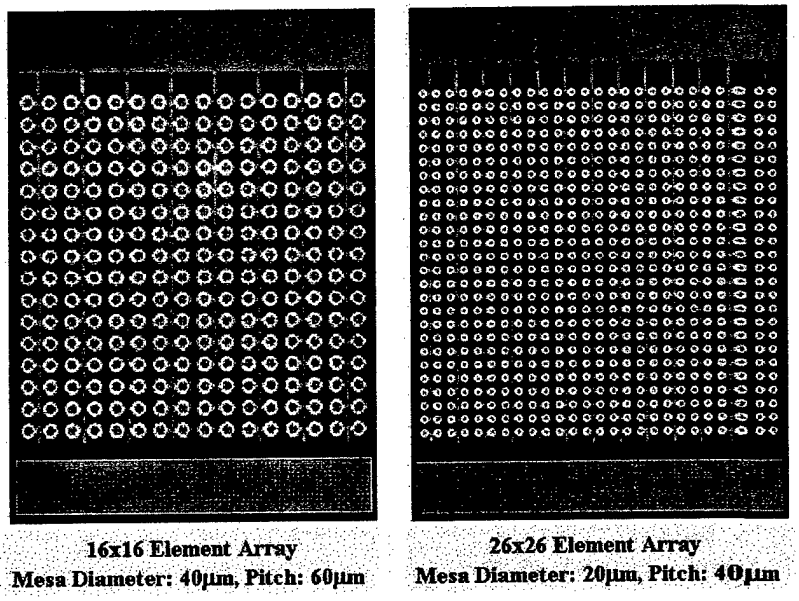

Fig. 16: Vertically-integrated low-power phototransceiver arrays.

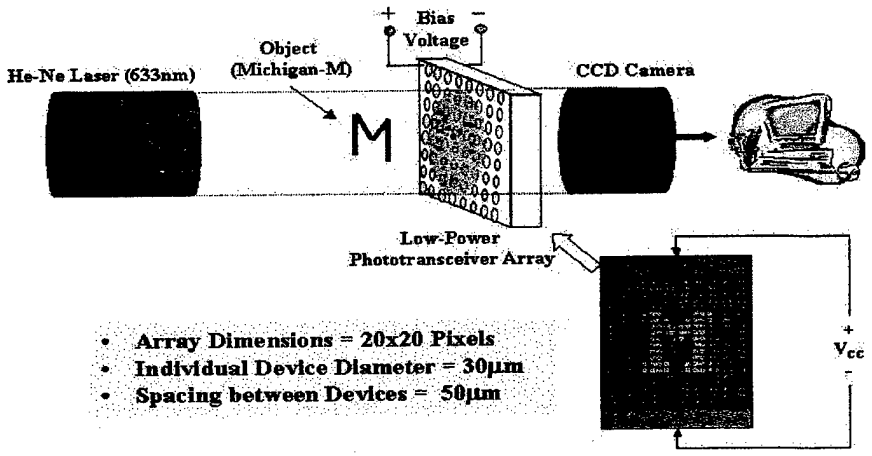

Fig. 17: Imaging experimental setup.

Imaging experiments were conducted with the arrays wired bonded and mounted on an optically transparent carrier. Illumination was provided with a 633 nm light from a

He-Ne laser. The output image at 980nm was recorded by a CCD-based near-field measurement system. The experimental setup is illustrated in Fig. 17.

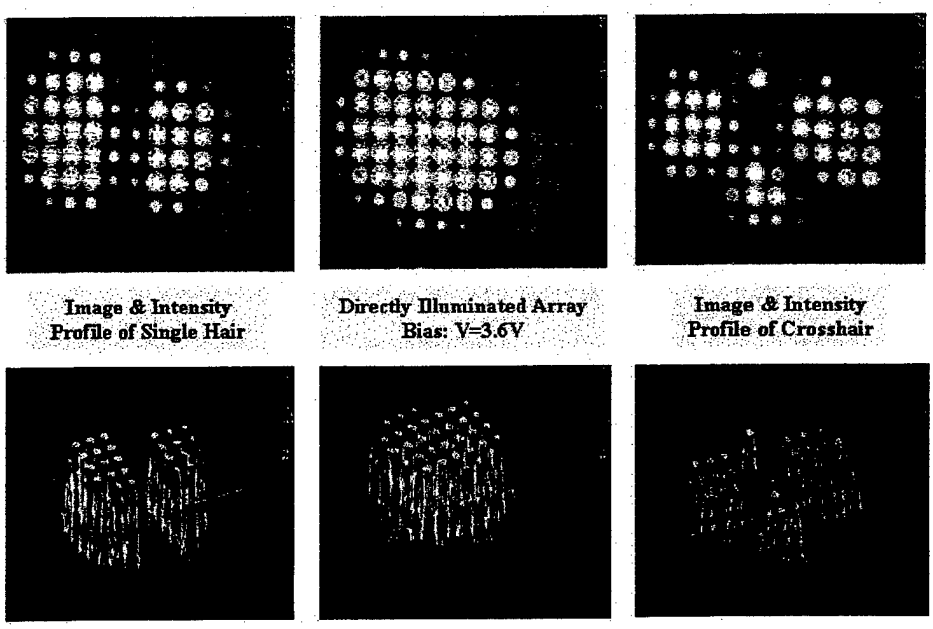

Fig. 18: Image and intensity profile of a single and cross-hair from low-power phototransceiver 20x20 element array.

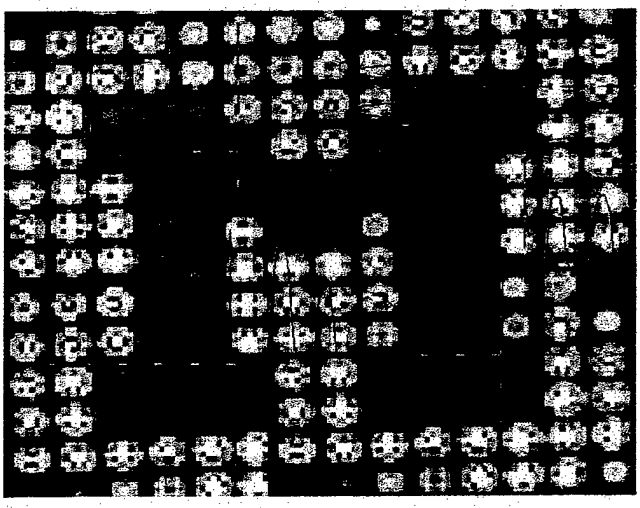

Fig. 19: Image of Michigan "M" from low-power phototransceiver 20x20 element array.

The image of a single and cross-hair as seen from the 20x20 element phototransceiver arrays biased at 3.6V is shown in Fig. 18. The individual

phototransceivers are 30μm in diameter and are spaced 50μm from each other. As can be seen, the image intensity is highest in the center and decreases towards the edge. This is due to non-uniform illumination of the array since the input laser beam from He-Ne laser has a Gaussian intensity distribution profile. With uniform illumination, a uniform intensity output image can be expected, since the array has very high uniformity. The image of a Michigan "M" from the same array similarly biased is seen in Fig. 19. The arrays, thus, demonstrate excellent imaging capability.

2.7. HIGH POWER PHOTOTRANSCEIVER

Since micromachined optics will limit the speed of image collection on a focal plane array to less than 10MHz, the low-power phototransceivers do not require large operational bandwidth. The overall bandwidth of the system can be enhanced in a subsequent stage using time-division multiplexing and having a high-speed phototransceiver array as the next stage in optoelectronic conversion. Power dissipation is not a crucial element in this array since each phototransceiver circuit will process information from several low-power phototransceivers in a parallel to serial conversion. Therefore, for all practical purposes, the high-power phototransceivers are similar to OEICs used in lightwave communication. In the present project we designed, fabricated and characterized *monolithically integrated* high-power phototransceivers the first time.

A high-power phototransceiver operating at 1.55μm consisting of a monolithically integrated photoreceiver and laser modulator-driver is demonstrated with an optical-to-optical small-signal –3dB bandwidth of 3.1GHz. The transceiver circuit exhibited a gain of 3.3dB and total power dissipation of 240mW. Two configurations of the photoreceiver-modulator circuit were fabricated. The small-signal optical-to-electrical bandwidth of the two circuits was measured to be 8.2GHz and 6.6GHz with 3.3dB and 6.3dB gain, respectively. The photoreceiver-modulator circuit is used to modulate an external single-mode ridge-waveguide tunneling-injection quantum well laser. The laser is driven by a monolithically-integrated driver that is built onto the same chip.

The photoreceiver circuit consists of a 10x12μm photodiode that converts input optical signal into electrical signal i.e. current, which is the input to the transimpedance amplifier. The transimpedance amplifier consists of a two-stage HBT circuit with a feedback gain resistance from the base of stage-1 to the collector of stage-2 as shown in Fig. 20. The gain and bandwidth of the 2-stage transimpedance-amplifier is tuned with the feedback resistance, R_F and peaking inductance L_1, respectively. The stage-3 is the laser modulator, which acts as the voltage-to-current in order to modulate the current through the laser diode. The laser is driven by an on-chip three-transistor Wilson current source.

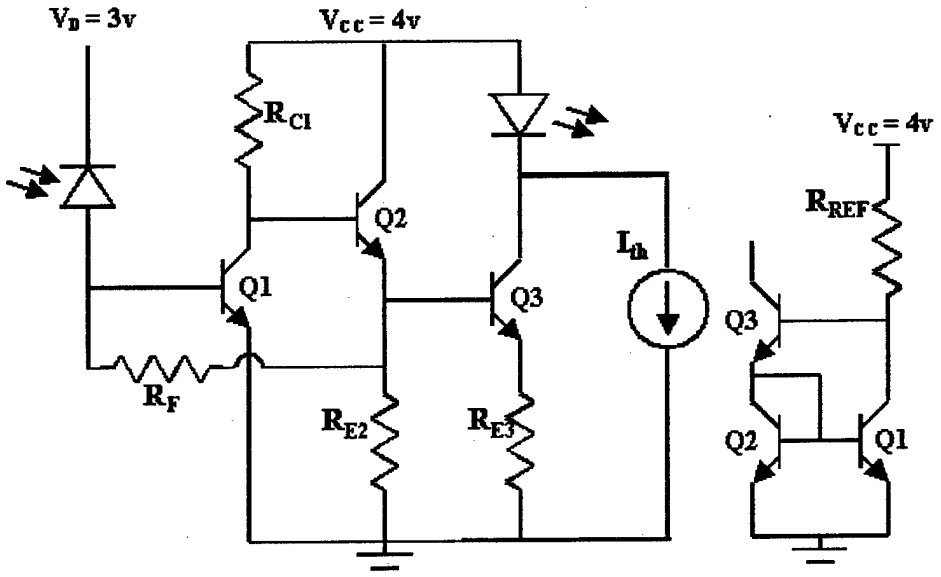

Fig. 20: Circuit Schematic of the high-power phototransceiver consisting of the front-end photoreceiver, current modulator, laser driver (current source) and the laser.

For testing the photoreceiver-laser driver OEIC, a 1.55μm strained multi-quantum well laser heterostructure was grown by metal-organic chemical vapor deposition (MOCVD) on (001) InP substrate. Single-mode ridge-waveguide lasers 200 to 400μm long, with 3μm-wide ridges, were formed by self-aligned reactive ion etching (RIE).

The discrete active devices and the different components of the OEIC were characterized to determine their dc and high-frequency performance. The HBTs exhibit dc current gain of 35 and common-emitter breakdown voltage of 4.5V. The high-

frequency performance of the transistors, measured with a HP8510 network analyzer, is characterized by f_T and f_{max} of 45GHz and 51GHz, respectively, for V_{CE} = 2.5V and I_B = 150μA. The photodiode has a responsivity of 0.45A/W with dark current lower than 10nA at a reverse-bias of 3V. The high-frequency performance of the photodiode was characterized with a HP83420-lightwave test set. The small-signal –3dB optical modulation bandwidth of the photodiode was measured to be larger than 20GHz, which is limited by the measurement system. The single-mode test laser with a 200μm long cavity exhibited a threshold current of 12mA and small-signal modulation bandwidth larger than 20GHz.

The monolithically integrated photoreceiver-laser driver OEIC was characterized to determine its high-frequency performance. The circuit is biased with a dc supply voltage of 4V. The photoreceiver stage exhibited a -3dB optical modulation bandwidth of 7GHz as seen in the frequency response characteristics of Fig. 21. The small-signal electrical bandwidth of the entire OEIC was determined from two-port S-parameter measurements using the network analyzer. The measured frequency response is shown in Fig. 22. The flatband gain and –3dB bandwidth are 4dB and 8.2GHz, respectively. This value of bandwidth is close to the design value. We believe that the bandwidth is largely limited by the frequency response of the HBTs and by parasitics. The eye-diagram of the OEIC, recorded at 10Gbps with a 32-bit NRZ pseudorandom binary stream (PRBS), is shown in the inset of Fig. 22. The eye-diagram is completely open, with minimal jitter.

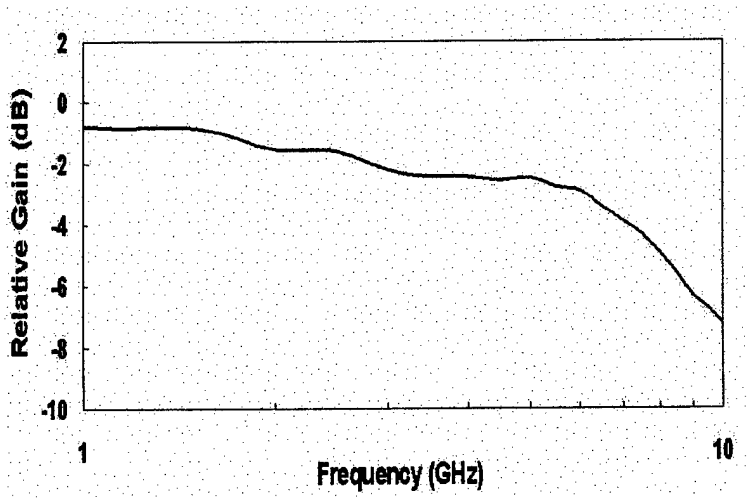

Fig. 21: Optical modulation response of PIN-HBT photoreceiver OEIC.

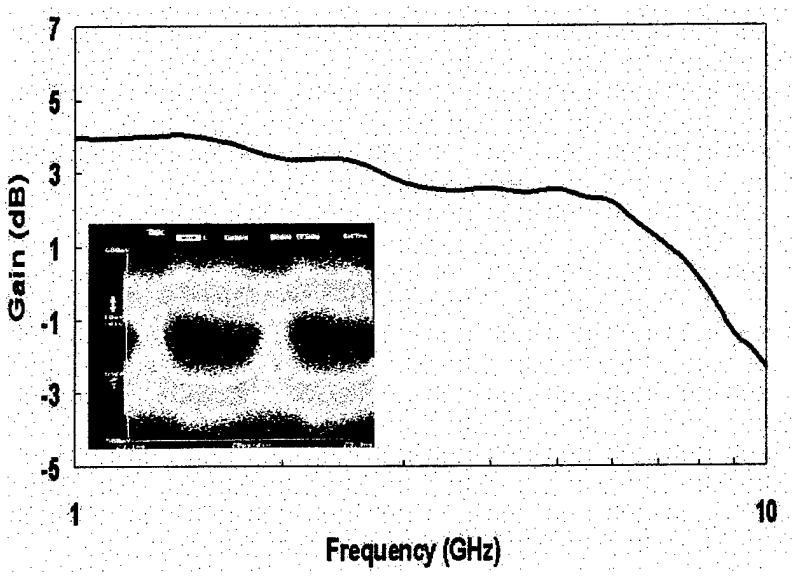

Fig. 22: Electrical gain v/s bandwidth of PIN-HBT photoreceiver-laser driver OEIC. Inset shows the eye-diagram at 10Gbps operation.

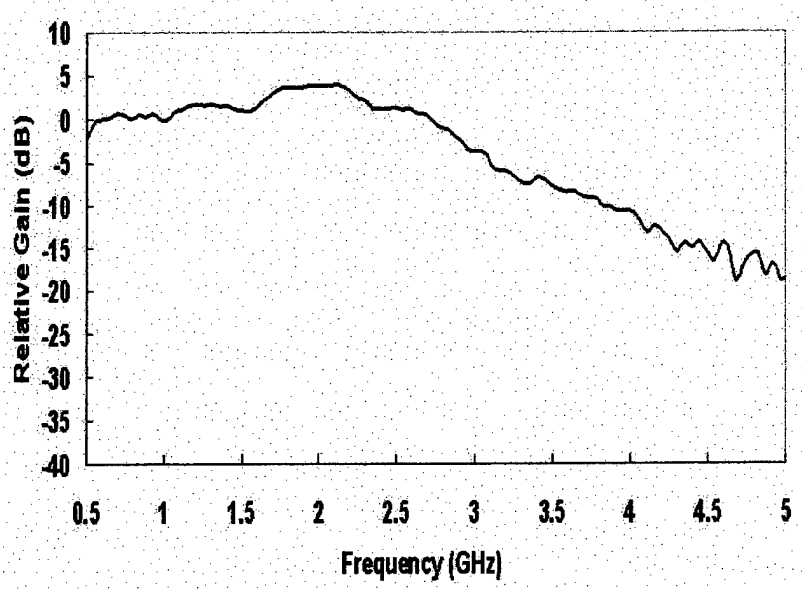

Fig. 23: Optical modulation response of PIN-HBT photoreceiver-laser driver OEIC.

Finally, the photoreceiver-laser driver OEIC was tested with the single-mode high-speed 1.55μm laser. The high-frequency electrical output of the OEIC, resulting from the high-frequency optical excitation (1.55μm) of the lightwave test set, together with the dc output of the laser driver were applied externally through a bias-T to the laser. The modulation response of the laser is shown in Fig. 23. The total power dissipation of the OEIC, including the dc drive current of the laser, is 240mW at a bias voltage of 4V.

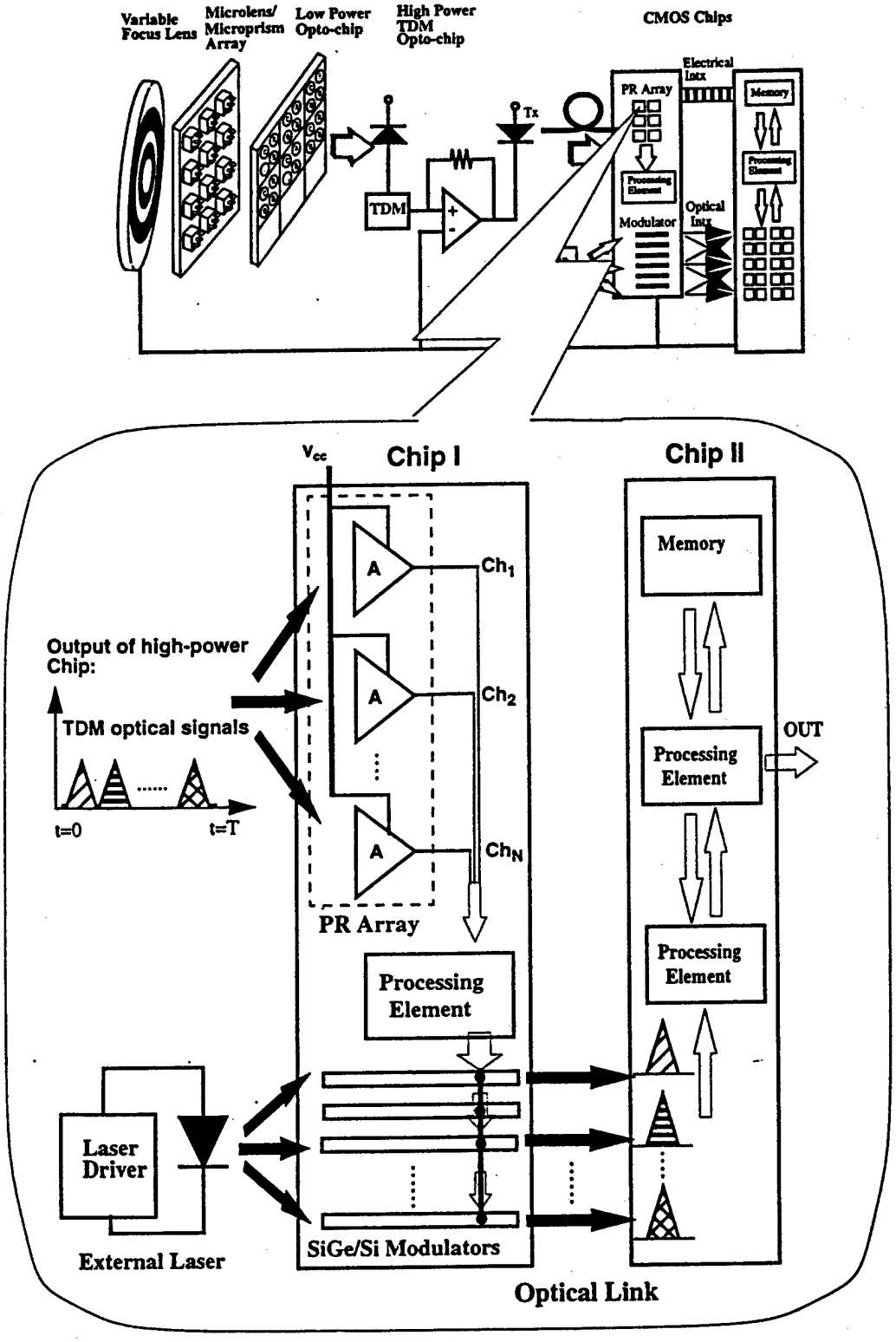

Fig. 24: Architecture of the CMOS processing chip. The figure illustrates the role of SiGe photoreceivers in the architecture.

2.8. SIGNAL PROCESSING WITH SI-BASED OEICS

From the technological point of view, Si-based optoelectronic devices are of great interest for densely-packed free-space interconnects and time division multiplexing (TDM) systems. Cost, reliability and compatibility with CMOS technology are the key factors. Besides low cost and high reliability, Si technology provides very large scale integration complexity where dense arrays of receivers, modulators and switching circuits can be fabricated on a single chip. In the design and realization of the optoelectronic eye, the SiGe-Si photoreceiver array can directly interface with low-voltage CMOS circuits and can be designed for massively parallel application where low power dissipation and low crosstalk are needed. An optical-to-electrical space division multiplexing scheme can be realized with the photoreceiver array. Because processing images requires extraordinary high signal bandwidth and massive parallel feedforward and feedback channels with multiple fanouts between the processing elements, it would be advantageous to implement interconnects between the CMOS chips with an external laser, SiGe/Si light modulators and SiGe/Si photoreceiver arrays. The integration of modulators and photoreceivers significantly improves the performance of the system.

2.8.1. SiGe/Si Photoreceivers

Monolithically integrated photoreceivers consisting of the three-stage transimpedance amplifier, inductor and a p+/n/n+ photodiode were designed and fabricated. The photoreceivers were designed to operate at a wavelength of 0.85μm. The fabricated p-n photodiode with AR coating exhibits a breakdown voltage as high as -20V and leakage current less than 150nA at -2V. The responsivity of the photodiode is measured to be 0.3A/W at 880nm. The bandwidth of the photoreceiver was measured using a high-speed single-mode edge emitting GaAs laser (λ = 880nm) and HP8593A spectrum analyzer. The laser was modulated with a HP8350 sweep oscillator and the light was coupled into a single mode fiber. The modulated light was fed into the photodiode with a tapered optical fiber probe and the electrical response of the photoreceiver was measured by a spectrum analyzer. The highest measured bandwidth of the photoreceiver,

which is limited by the bandwidth of the photodiode, is 0.8GHz at 2V applied bias. This relatively low bandwidth is attributed to the slow diffusion mechanism in the subcollector region. The total photocurrent of the p-n photodiode consists of fast (drift) and slow(diffusion) components, which arise from the carrier generation in the depletion region and subcollector region of the photodiode structure, respectively. The measured eye diagram of the photoreceiver at bit rate of 1Gpbs is shown. The diagram shows clear eye open with percentage jitter and eye closure of 45% and 54%, respectively.

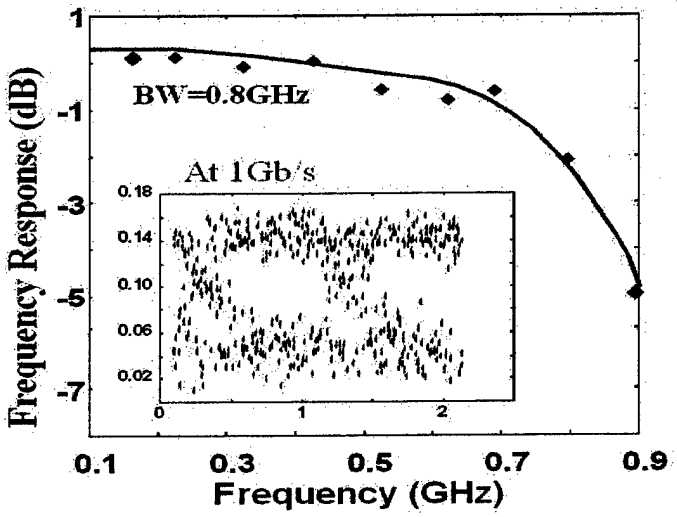

Fig. 25: Frequency response of single channel photoreceiver. Inset shows eye diagram at 1Gbps.

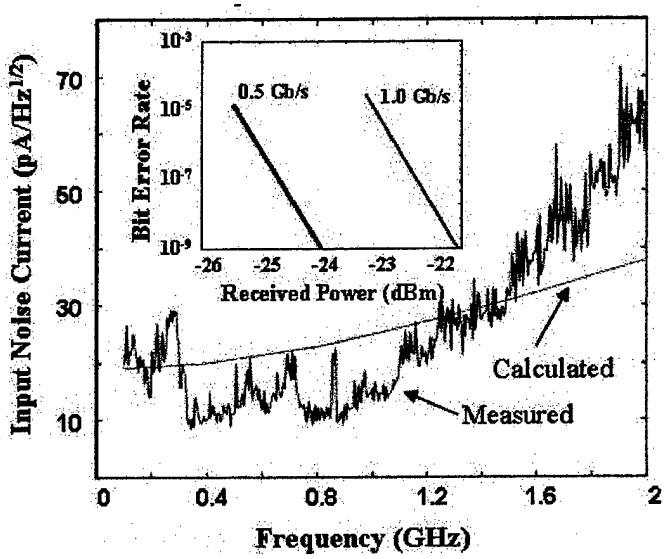

Fig. 26: Measured and calculated photoreceiver input noise. Inset shows calculated BER at 0.5 and 1.0Gbps.

The equivalent noise current at the input was estimated by summing all noise sources. Thermal noise generated from the biasing resistors and shot noise, generated from base and collector currents of the HBTs were considered in the calculation. The calculation was carried out with the help of HSPICE using typical operating conditions of the HBTs, the photodiode and the feedback and bias resistors. The receiver sensitivity can be expressed as:

$$\eta\overline{P} = \frac{h\nu}{q} Q\sqrt{\langle i_n^2 \rangle}$$

where $\langle i_n^2 \rangle$ represents the sum of the mean squared values of all physical sources of device and circuit noise at the input of the circuit. The photoreceiver sensitivity is estimated to be -23dBm at 0.5Gbps for BER of 10^{-9}.

2.8.2. Multichannel Photoreceiver Arrays

Multichannel (8x1) photoreceiver arrays were designed and fabricated in a similar manner, as described in the previous section. The array size is 1.5x2 mm with interchannel spacing of 250μm. Good uniformity in the frequency response between individual photoreceiver elements is achieved. The eight channels show near-identical frequency response with -3dB bandwidth of 0.7±0.1GHz and an average transimpedance gain of 44±2dBΩ. The yield of the discrete devices is more than 90%, which results in about 50% yield for the fabricated arrays. The crosstalk was measured by photoexciting channel 4 and measuring the RF output at the adjacent channels. Special care is taken to ensure that there is no feedforward to the output in the absence of the input optical signal. The maximum crosstalk, measured within the 0.8GHz bandwidth of the photoreceiver, is less than -26dB.

The overall crosstalk is a combination of optical and electrical crosstalk. The optical crosstalk was minimized by the experimental arrangement. The crosstalk signal from channel 5 is only 1dB higher than from channel 8. Electrical crosstalk is a result of

microwave power propagating through the interconnection lines and the parasitic capacitors and therefore the circuit layout may be important.

An optical-to-electrical space division multiplexing system can be realized with the photoreceiver array. The concept is illustrated in the following diagram. A time division multiplexed (TDM) signal is superimposed on the laser driver circuitry and the output optical TDM signal is distributed by fiber or holographic means to the n-channel photoreceiver array. The TDM electrical signal is also used to sequentially trigger n-channels of photoreceiver biasing (V_{CC}) signals. Each channel of the array is biased with pulses having a period of T and duty cycle T_d. For incoming N light signals, each signal can be routed through a specific photoreceiver channel in a short time, T_d, which is determined by the photoreceiver bandwidth. It should be noted that the power dissipation in the photoreceiver array is significantly reduced in the system. To test this scheme, only one channel (4) is pulse-biased. An optical signal from a GaAs laser (λ = 0.88μm) modulated at f_m = 0.5GHz, is coupled into channel 4 and the photoreceiver output is monitored by a spectrum analyzer. The signal was detected for various values of T and T_d with minimal noise and crosstalk. In this scheme, the choice of T and T_d would depend on N and f_m, where N is the number of photoreceiver channels.

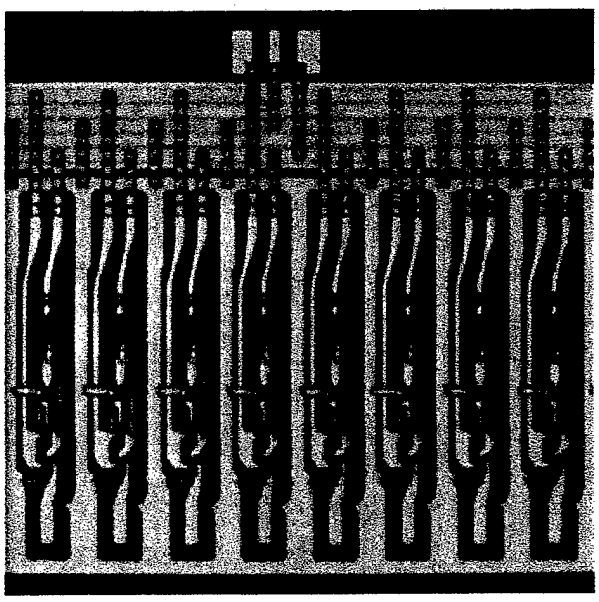

Fig. 27: Photomicrograph of monolithically integrated 8-channel SiGe-Si PIN/HBT photoreceiver array.

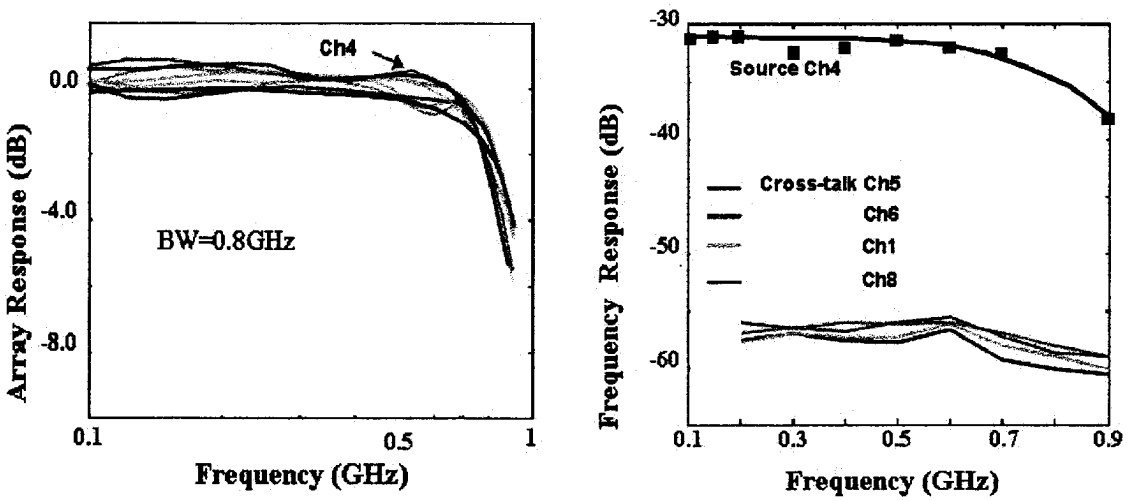

Fig. 28: (a) Measured individual channel frequency response of the 8-channel array (b) Measured frequency response of channel-4 and adjacent channel crosstalk.

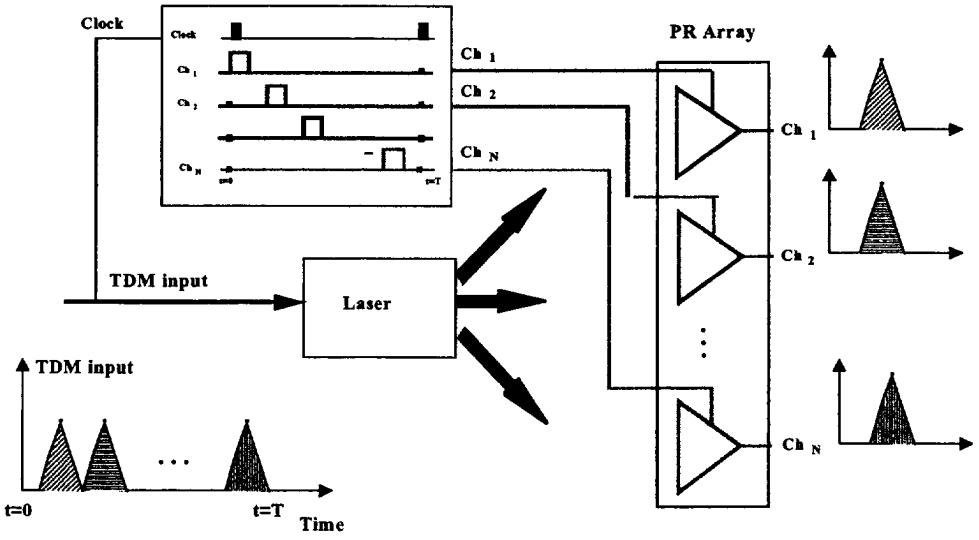

(a)

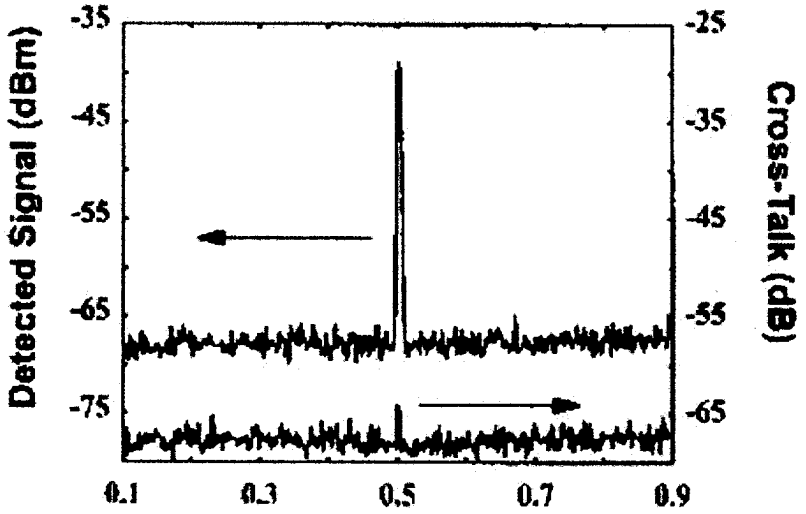

(b)

Fig. 29: (a) An optical-to-electrical space division multiplexing scheme using a multichannel photoreceiver array (b) Measured individual channel response and adjacent channel crosstalk.

2.8.3. SiGe/Si Quantum Well Optical Modulator for Optical Data Links

To alleviate the connectivity and fan-out restrictions in the optoelectronic eye, it is very important to introduce optoelectronic parallel processing components. Optical interconnects can provide higher clock speed and circuit densities. Since lasers cannot be fabricated with Si materials, the intra and interchip data links can be implemented with SiGe-Si modulators and photoreceivers.

Quantum Well modulators based on the Stark effect, commonly known as Quantum Confined Stark Effect (QCSE) modulators have been successfully demonstrated with III-V based quantum well heterostructures. The operation of pseudomorphic SiGe-Si quantum wells has been largely unsuccessful. The reason for this originates from the small conduction band offset of SiGe/Si heterostructure. The electron wavefunction is very weakly localized in the conduction band even under zero field conditions. With the application of even a small transverse electric field, the exciton binding energy is sharply reduced, leading to a blue shift in the transition energy. This blue shift more than balances the field induced red shift due to the Stark effect. As a

result, the QCSE is not observed in SiGe-Si modulators. It might be possible to make modulators with SiGe-Si type II quantum wells because of the very large electron effective mass ($0.92m_o$) and consequently large exciton binding energy in these structures. However, such devices are yet to be realized.

Interestingly, however, the weak confinement of the electron wavefunction in the SiGe-Si type I quantum well can be utilized to realized low-voltage modulator. It may be noted that the Si and Ge lattices are centro-symmetric and therefore exhibit no electro-optic effect. In SiGe-Si quantum wells, photons with energy equal to the electron-heavy hole transition energy will be absorbed with phonon participation under flat-band conditions. A small transverse electric field will reduce the oscillator strength of this transition due to delocalization of the electron wavefunction (while the heavy hole remains confined) and the absorption will be reduced to small value. Thus, modulation will be dependent on controlling the overlap integral between the electron and hole wavefunctions. It is important to note that unlike the QCSE electroabsorption modulator, the photon energy of choice in this scheme for optimal operation should be higher than the bandgap of the SiGe well. We have realized such a modulator in another program of research and, simply for completeness, the modulator heterostructure and some calculated data are shown in Fig. 30 through Fig. 32.

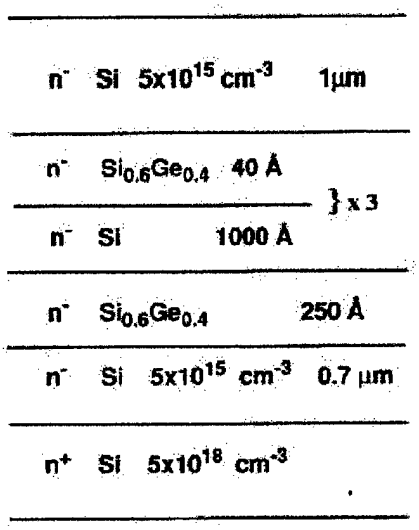

Fig. 30: Heterostructure of Si-SiGe QW modulator.

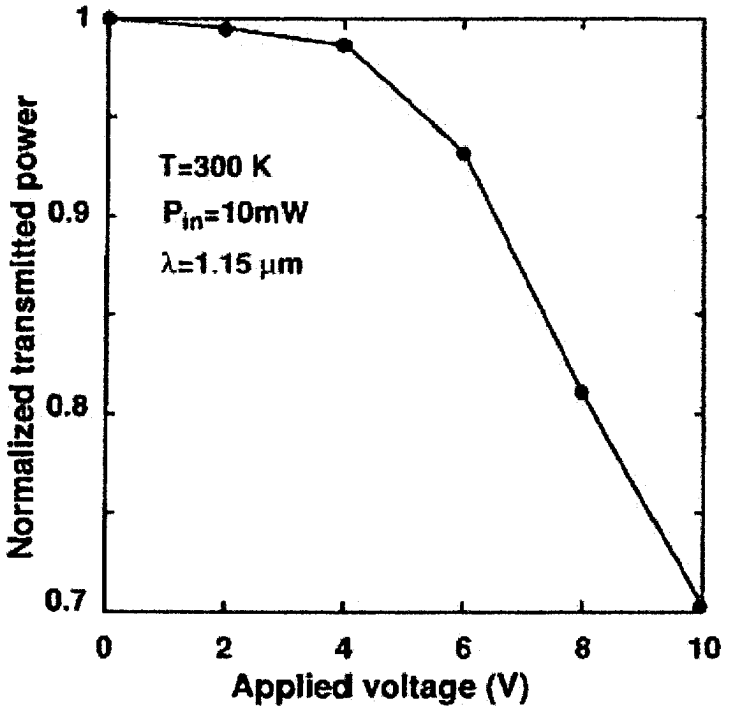

Fig. 31: Measured transmission as a function of applied bias in a 100μm-long device.

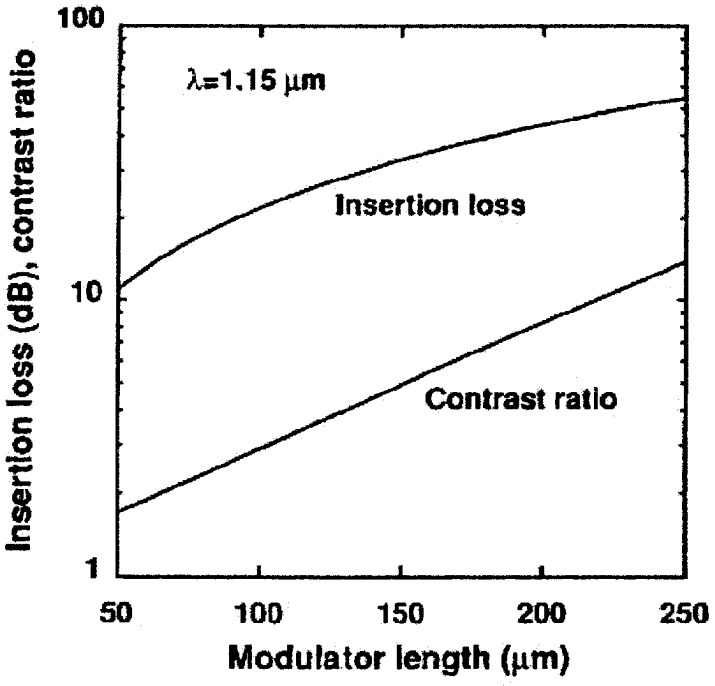

Fig. 32: Calculated contrast ratio and insertion loss of QW modulator as a function of the modulator length.

3. LIST OF PUBLICATIONS

3.1. ARCHIVAL JOURNALS

1. "Extended Wavelength (1.0 to 1.3μm) InGaAs/GaAs Quantum Dot GaAs-Based Vertical-Cavity Surface-Emitting and Lateral-Cavity Edge-Emitting Lasers", Int. *J. High Speed Electr. Syst.*, 9 (4), 133, 1998.

2. "Ground State Lasing from a Quantum Dot Oxide-Confined Certical-cavity Surface-Emitting Laser", *Appl. Phys. Lett.*, **75**, 22, 1999.

3. "Intracavity Contacts for Low Threshold Oxide-Confined Vertical-Cavity Surface-Emitting Lasers", *IEEE Phot. Tech. Lett.*, **11**, 934, 1999.

4. "Structural and Luminescence Characteristics of Cycled Submonolayer InAs/GaAs Quantum Dots with Room Temperature Emission at 1.3μm", S. Krishna, D. Zhu, J. Xu, K. Linder, O. Qasaimeh, and P. Bhattacharya, *J. Appl. Phys.*, 86 (11), 1999.

5. "GaAs/$Al_{0.3}Ga_{0.7}As$ Multiquantum Well Dual Focus Fresnel Lens-Modulator", J. Xu, O. Qasaimeh, P. Bhattacharya, D. Huffaker and D. Deppe, *Electron. Lett.*, 36 (1), 2000.

6. "Monolithically Integrated Low-Power Phototransceiver Incorporating InGaAs/GaAs Quantum Dot Microcavity LED and Modulated Barrier Photodiode", O. Qasaimeh, W-D. Zhou, P. Bhattacharya, D. Huffaker and D.G. Deppe, *Electron. Lett*, 36 (23), 1955, 2000.

7. "Monolithically Integrated Low-Power Phototransceiver Incorporating Microcavity LEDs and Multiquantum Well Phototransistors," O. Qasaimeh, W. Zhou, and P. Bhattacharya, *IEEE Phot. Tech. Lett*, 12, 1683, 2000.

8. "Obtaining High Efficiency at Low Power Using a Quantum Dot Microcavity Light Emitting Diode", *IEEE J. Quantum Electron.*, 36, 674, 2000.

9. "Ultra-Low Threshold Cryogenic Vertical-Cavity Surface-Emitting Laser", Z. Zou, D.L. Huffaker, and D.G. Deppe, *IEEE Phot. Tech. Lett.*, 12, 1, 2000.

10. "InGaAs Quantum Dot Lasers with Sub-mA Thresholds and Ultra-Low Threshold Current Density Below Room Temperature", G. Park, O.B. Shchekin, D.L. Huffaker, and D.G. Deppe, *Electron. Lett.*, 36, 1283, 2000.

11. "Monolithically Integrated Multichannel SiGe/Si PIN-HBT Photoreceiver Arrays," O. Qasaimeh, Z. Ma, P. Bhattacharya, and E. Croke, *J. Lightwave Technol.*, 18, 1548, 2000.

12. "Monolithically Integrated Low-Power Phototransceivers for Optoelectronic Parallel Sensing and Processing Applications," O. Qasaimeh, W. Zhou, P. Bhattacharya, D. Huffaker, and D. Deppe, *J. Lightwave Technol.*, 19, 546, 2001.

13. "Apertured Quantum Dot Microcavity Light Emitting Diodes", Z. Zou, H. Chen, and D.G. Deppe, *Appl. Phys. Lett.*, 77, 2001.

14. "InP-Based Cylindrical Microcavity Light Emitting Diodes," W. Zhou, P. Bhattacharya, O. Qasaimeh, *J. Quant. Electron.*, 37, 48, 2001.

15. "Characteristics of a Photonic Bandgap Single Defect Microcavity Electroluminescent Device", W. D. Zhou, J. Sabarinathan, P. Bhattacharya, B. Kochman, E. Berg, P.C. Yu, and S. Pang, *J. Quant. Electron.*, 37, 1135, 2001.

16. "Low-Power Phototransceiver Arrays with Vertically Integrated Resonant-Cavity LEDs and Heterostructure Phototransistors", W.-D., Zhou, S. Pradhan, P. Bhattacharya, W. K. Liu, and D. Lubyshev, *IEEE Photon. Technol. Lett.*, 13, 1218, 2001.

17. "High Differential Efficiency (>16%) Quantum Dot Microcavity Light Emitting Diodes", H. Chen, Z. Zou, and D.G. Deppe, *Appl. Phys. Lett.*, 80, 350, 2002.

18. "A Monolithically Integrated 1.55μm Photoreceiver-Laser Driver Optoelectronic Integrated Circuit", S. Pradhan, P. Bhattacharya, and W.K. Liu, *Electron. Lett.*, 38, 987, 2002.

19. "Room-Temperature Continuous-Wave Operation of GaAs-Based Vertical Cavity Surface Emitting Laser Based on p-Type GaAs/Air Mirror", Q. Mo, H. Chen, Z. Huang,, O.B. Shchekin, C. Cao, S. Lipson, and D.G. Deppe, *Electron. Lett.*, 39, (6), 525, 2003.

3.2. CONFERENCE PRESENTATIONS

1. "A Representation of Specular Appearance", S. Lin and S. W. Lee, Proc. IEEE International Conference on Computer Vision, Kerkyra, Greece, September, 1999.

2. "Generation of Diffuse and Specular Appearance from Photometric Images", S. Lin and S. W. Lee, Proc. IEEE International Conference on Computer Vision, Kerkyra, Greece, September, 1999.

3. "Spectral Gradient: A Material Descriptor Invariant to Geometry and Incident Illumination", E. Angelopoulou, S. W. Lee and R. Bajcsy, Proc. IEEE International Conference on Computer Vision, Kerkyra, Greece, September, 1999.

4. "Spectro-Spatial Gradients for Color-Based Object Recognition and Index Proc. International ing", D. Berwick and S.W. Lee, Conference on Computer Analysis of Images and Patterns, Ljubljana, Slovenia, September, 1999.

5. "An Appearance Representation for Multiple reflection Components", S. Lin and S.W. Lee, IEEE Conference on Computer Vision and Pattern Recognition, Hilton Head Island, SC, June 2000.

6. "Ultra-low Power Monolithically Integrated InGaAs/GaAs Phototransceiver Incorporating a Modulated Barrier Photodiode and A Quantum Dot Microcavity LED", O. Qasaimeh, W. Zhou, P. Bhattacharya, D. Huffaker, and D. Deppe, IEEE Lasers and Electro-Optics Society (LEOS) Annual Meeting, Puerto Rico, November 2000.

7. "Phototransceiver Arrays with Phototransistors and Resonant Cavity Light Emitting Diodes Vertically Integrated with Tunnel Junctions", W.D. Zhou, S. Pradhan, P. Bhattacharya, W.K. Liu, and D. Lubyshev, IEEE Lasers and Electro-Optics Society (LEOS) Annual Meeting, San Diego, CA, November 2001.

8. "Increasing the Discrimination Power of Spectral Spatial Gradients", D. Berwick and S.W. Lee, IEEE Conference on Computer Vision and Pattern Recognition, Kauai, Hawaii, December 2001.

9. "A Low Voltage Tiltable Microplatform Using Bent-Beam Actuation", Y. Xie and C.T.-C. Nguyen, 2002 Solid-State Sensor, Actuator, and Microsystems Workshop, Hilton Head, SC, June 2002.

3.3. INVITED AND PLENARY TALKS

1. "Microcavity Physics Based on Quantum Dot Light Emitters", (INVITED), D.G. Deppe and D.L. Huffaker, Optical Society of America Annual Meeting, Baltimore, October 1998.

2. "Oxide-Confined Vertical Cavity Surface Emitting Lasers with Quantum Well and Quantum Dot Active Regions", (INVITED), D.L. Huffaker, and D.G. Deppe, Optical Society of America Annual Meeting, Baltimore, MD 1998.

3. "Dielectric Apertures for Mode Control in Low Threshold and Single Mode Vertical Cavity Surface-Emitting Lasers", (INVITED), D.G. Deppe, D. L.

Huffaker, T.-H. Oh, and Z. Zou, IEEE Lasers and Electro-Optics Society Annual Meeting, Orlando, FL 1998.

4. "Selectively Oxidized Dielectric Apertures and Mirrors for Low Threshold VCSELs and Spontaneous Light Emitters", (INVITED), D.G. Deppe, D. L. Huffaker, L.A. Graham, S. Csutak, and Q. Deng, Spring Meeting, San Francisco, CA 1999.

5. "Ground State lasing at 1.07μm from InGaAs/GaAs QD VCSELs", (INVITED), IEEE Summer Topicals on VCSELs and Microcavities, San Diego, CA 1999.

6. "Reduced Cavity Loss for Ultra-Low Threshold Vertical Cavity Surface Emitting Lasers", D. L. Huffaker, Z. Zou, and D.G. Deppe, IEEE Lasers and Electro-Optics Society Annual Meeting, San Francisco, CA 1999.

7. "Quantum Dots for 1.1 to 1.3 micron VCSELs and Microcavities", (INVITED), D.G. Deppe, D. L. Huffaker, G. Park, O. Shchekin, and Z. Zou, SPIE Photonics West, San Jose, CA 2000.

8. "Advances in Vertical-Cavity Surface-Emitting Lasers and Microcavities", (INVITED), D.G. Deppe, International Symposium on ultra-Parallel Optoelectronics, Kawasaki-city, Japan 2000.

9. "Shape Engineering to Improve the Threshold Temperature Dependence in Quantum Dot Lasers", O.B. Shchekin, 42nd Electronic Materials Conference, Denver, CO 2000.

10. "Monolithically Integrated Low-Power Phototransistor Incorporating Microcavity LEDs and Multiquantum well phototransistors", Q. Qasaimeh, W. Zhou, P. Bhattacharya, D. Huffaker, and D. Deppe, Device Research Conference, Denver, CO 2000.

11. "Temperature Dependence of Quantum Dot Lasers", (INVITED) SPIE Optoelectronic Materials and Devices II, Taipei, Taiwan, July 2000.

12. "Ultra-Low Power Monolithically Integrated InGaAs/GaAs Phototransceiver Incorporating at Modulated Barrier Photodiode and a Quantum Dot Microcavity LED", Q. Qasaimeh, W. Zhou, P. Bhattacharya, D. Huffaker, and D. Deppe 13th Annual Meeting IEEE Lasers and Electro-Optics Society Annual Meeting, Rio Grande, Puerto Rico, 2000.

13. "Shape Engineering of Quantum Dots for High Speed Laser and Microcavity Light Emitters", D.G. Deppe, 10th Seoul International Symposium on the Physics of Semiconductors and Applications, Cheju Island, Korea, November, 2000.

14. "Carrier Dynamics of InGaAs/GaAs Quantum Dots for Low Power Microcavity Lasers and Light Emitters", (INVITED), D.G. Deppe, Annual Conference on Physics of Quantum Electronics, Snowbird, UT, January 2001.

15. "High Efficiency Quantum Dot Microcavity Light Emitter", Z. Zou, H. Chen and D.G. Deppe, Optical Society of America Integrated Photonics Research Topical Meeting, Monterey, CA, June 2001.

16. "Carrier Dynamics and Device Characteristics of Quantum Dot Lasers and Microcavity Light Emitters", D.G. Deppe, C. Cao, O.B. Shchekin, Z. Zou, H. Chen, T.F. Boggess, L. Zhang, and K. Gundodgu, 10th International Conference on Modulated Semiconductor Structures, Linz, Austria, July 2001.

17. "Exciton Carrier Dynamics of Quantum Dots and Their Application to lasers and Microcavity Light Emitters", (INVITED), D.G. Deppe, C. Cao, O.B. Shchekin, Z. Zou, H. Chen, T.F. Boggess, L. Zhang, and K. Gundodgu, Alaska Meeting on Fundamental Optical Processes in Semiconductors, Anchorage, Alaska, August 2001.

18. "Electrically Injected Microcavity Devices for Single Photon Sources", (INVITED), D.G. Deppe, H. Chen, Z. Zou, C. Cao, and O. Shchekin, Annual Conference on Physics of Quantum Electronics, Snowbird, UT, January 2002.

19. "Ultra-Low Power High Efficiency Quantum Dot Microcavity Light Emitters", (INVITED), D.G. Deppe, H. Chen, Z. Zou, C. Cao, and O. Shchekin, Advanced Workshop on Frontiers in Electronics (WOFE) St. Croix, Virgin Islands, January 2002.

20. "Quantum Dots for Lasers and Microcavity Devices", (INVITED), D.G. Deppe, O.B. Shchekin, Q. Mo, C. Cao, Z. Zou, and H. Chen, Vertical-Cavity Surface-Emitting Lasers VI-Photonics West, San Jose, CA, January 2002.

21. "Quantum Dot Lasers for Lasers, Photonic Crystals and Other Microcavity Light Emitters", (INVITED), LEOS Benelux Photonic Crystal Workshop, Chent, Belgium, May 2002.

22. "Low Power Phototransceivers and Phototransceiver Arrays for High Density Optical Interconnect and Imaging Applications", (INVITED), P. Bhattacharya, S. Pradhan, W.-D. Zhou, and O. Qasaimeh, First Symposium on Integrated Optoelectronics at the 201st Meeting of the Electrochemical Society, Philadelphia, PA, May 2002.

4. LIST OF TECHNICAL REPORTS SUBMITTED TO ARO

1. Interim progress report, 6/1/98-12/31/98

2. Interim progress report 1/1/99-12/31/99

3. Interim progress report, 1/1/00-12/31/00

4. Interim progress report, 1/1/01-12/31/01

5. Interim progress report, 1/1/02-12/31/02

5. NEWSLETTERS

November 1999
February 2000
April 2000
June 2000
August 2000
December 2000
April 2001
November 2001
April 2002
November 2002

6. PARTICIPATING SCIENTIFIC PERSONNEL

6.1. CO-PRINCIPAL INVESTIGATORS:

Professor Pallab Bhattacharya, University of Michigan

Professor Dennis Deppe, UT-Austin

Dr. Jack East, University of Michigan

Professor George I. Haddad, University of Michigan

Professor Sang Lee, University of Michigan

Professor Clark Nguyen, University of Michigan

6.2. POST-DOCTORAL FELLOWS:

Dr. S. Chakrabarti, University of Michigan

Dr. D. Huffaker, University of Texas at Austin

Dr. X. Liu, University of Michigan

Dr. J. Sun, University of Michigan

Dr. K. Yang, University of Michigan

Dr. S. Zaytsev, University of Texas at Austin

Dr. D. Zhu, University of Michigan

6.3. GRADUATE STUDENT RESEARCH ASSISTANTS:

E. Berg	Q. Mo
D. Berwick	G. Park
C. Cao	S. Pradhan
H. Chen	O. Qasaimeh
C. Fischer	J. Sabarinathan
S. Ghosh	J.M. Won
S. Govindaswamy	Y. Xie
H. Huang	J. Xu
Z. Huang	T. Ye
Z. Krishna	W-D. Zhou
S. Lin	Z. Zou
S. Lipson	

7. REPORT OF INVENTIONS

- Invention disclosure on "Bent-Beam Actuated Steerable Microplatform" was filed at the University of Michigan - Office of Technology on April 30, 2002.

8. DOCTORAL THESES

Zhengzhong Zou "GaAs-Based Quantum Dot Vertical-Cavity Surface-Emitting

	Lasers and Microcavity Surface-Emitting Lasers and Microcavity Light Emitting Diodes", University of Texas at Austin
Omar Qasaimeh	"Monolithically Integrated Low-Power Phototransceivers and Photoreceivers for Application in an Optoelectronic Eye", University of Michigan
Weidong Zhou	"Microcavity and Quantum Dot Light Sources for Optical Interconnects", University of Michigan
Stephen Lin	"Photometric Modeling of Specular and Diffuse Appearance", University of Michigan
Daniel Berwick	"A Framework for Color Image Indexing and Object Recognition: Spectral and Spectral Spatial Gradients", University of Michigan
Sameer Pradhan	"Optoelectronic Devices and Integrated Circuits for Imaging Applications", University of Michigan